



Universiteit Utrecht

Master Thesis

Novel interface engineered Na fast ion conductors for all-solid-state batteries

The influence of surface properties on the ion conduction of sodium nitrite and sodium nitrate based nanocomposites

M.E.T. van Ittersum, BSc.

4268814

January 31, 2020

Examiner: dr. P. Ngene

Second reader: prof. dr. P. E. de Jongh

Abstract

The energy demand is growing annually and at the same time the CO₂ emission needs to be reduced. Renewable energy sources are inevitable to fulfil both requirements. Given the intermittent nature of renewable energy sources, proper energy storage systems have to be developed. Batteries are promising for energy storage, given the wide application of lithium-ion battery these days. However, lithium is relatively scarce and therefore costly. As a consequence, cheap alternatives such as sodium ion batteries are investigated. Current sodium batteries operate at 300 °C due to a lack of good electrolytes. Therefore, a substantial amount of research is being carried out into investigating electrolytes. Solid-state electrolytes are promising electrolytes, since they are safer than liquid electrolytes. Unfortunately, solid-state electrolytes face other challenges, such as a low ion conductivity or a poor interface with the electrodes. In this work, an novel class of solid-state electrolytes based on low-cost sodium salts such as nitrites and nitrates was investigated. The main challenge for these materials is increasing their low ion conductivity. Therefore, this work focussed on increasing the ion conductivity by making nanocomposites of the sodium salts and metal oxides scaffolds. On top of that, it studied the effect of different metal oxides on the ion conductivity of the nanocomposites. Synthesis of nanocomposites of NaNO₂ and Al₂O₃, TiO₂, Nb₂O₅, Nb₃(PO₄)₅ and ZrO₂ via melt infiltration turned out successful, but the approach did not work for nanocomposites of NaNO₂ and SBA-15 (SiO₂). All nanocomposites showed an increase in ion conductivity compared to the pure salt, exceeding a 1000 fold increase for the NaNO₂@Al₂O₃ nanocomposite. Similar results were found for NaNO₃ based nanocomposites, showing that nanoconfinement is a promising method to boost the conductivity of sodium nitrites and nitrates. Preliminary results combining pyridine-FTIR, NH₃-TPD and a model study suggest a correlation between the increase in conductivity and the strength of the Lewis acid sites on the metal oxide. However, more research is required to exclude the influence of other properties, such as the porosity and the surface area of the scaffold, on the ion conductivity and to fully understand the origin of the boost in conductivity.

Contents

1	Introduction	12
2	Theory	14
2.1	Part I: Batteries	14
2.1.1	Introduction to batteries	14
2.1.2	Sodium batteries	15
2.1.3	Sodium electrolytes	16
2.2	Part II: Methods	18
2.2.1	Synthesis: Melt Infiltration	18
2.2.2	Analysis	18
2.2.2.1	Nitrogen Physisorption (N_2 -physisorption)	19
2.2.2.2	X-ray Diffraction (XRD)	19
2.2.2.3	Diffuse Reflectance Infrared Fourier Transform (DRIFTS)	20
2.2.2.4	Differential Scanning Calorimetry (DSC)	20
2.2.2.5	Pyridine Fourier Transformed Infrared Spectroscopy (pyridine-FTIR)	20
2.2.3	Ammonia temperature programmed desorption(NH_3 -TPD)	21
2.2.4	Electrochemical Impedance Spectroscopy (EIS)	21
3	Experimental Method	24
3.1	Synthesis	24
3.1.1	Scaffolds	24
3.1.2	Melt Infiltration	25
3.2	Analysis	25
3.2.1	N_2 -physisorption	25
3.2.2	XRD	26
3.2.3	DRIFTS	26
3.2.4	DSC	26
3.2.5	pyridine-FTIR	26
3.2.6	NH_3 -TPD	27
3.2.7	EIS	27
4	Results and Discussion	28
4.1	Part I: Nanocomposites of different compositions	28
4.1.1	Scaffolds	28
4.1.2	Nanocomposites	29
4.1.3	Conductivity	33
4.1.4	Summary	38
4.2	Part II: A systematic study	39

4.2.1	Scaffolds	39
4.2.2	Nanocomposites	39
4.2.3	Conductivity	40
4.2.4	Summary	42
5	Conclusions and Outlook	44
6	A Laymen’s Summary	46
	Acknowledgement	47
	Bibliography	49
	Appendix	55
6.1	A: Supporting information	56
6.1.1	NaNO ₂	56
6.1.2	NaNO ₃	60
6.2	B: List of samples	63
6.3	D: Excluded experiments	65

List of Figures

1.1	Schematic representation of the ideal energy grid, where energy is obtained from renewable energy sources, stored in energy storage systems to overcome the intermittent nature of renewable energy sources and finally supplied to the consumer.	12
2.1	Schematic representation of the first Li-ion battery (LiCoO_2 cathode, Li^+ electrolyte and graphite anode). Reprinted from Goodenough et al. ¹³	14
2.2	Schematic representation of a NaS battery with a molten Na anode, a S cathode and sodium β -alumina electrolyte. Reprinted from Dunn et al. ¹⁰	16
2.3	Schematic representation of a liquid droplet wetting a solid surface, with γ_{sv} the surface energy of the solid, γ_{lv} the surface energy of the liquid, γ_{sl} the surface energy of solid-liquid interface and θ_c the contact angle.	18
2.4	Schematic representation of X-ray diffraction. The X-ray beam (incident angle θ) is diffracted by the crystalline material with lattice spacing d .	19
2.5	Interactions of pyridine with Lewis and Brønsted acid sites	21
2.6	NyQuist plot: plot of the imaginary part of the impedance versus the real part. The non-zero intersection with the x-axis give the resistance R. Reprinted from Ern�. ⁵³	23
3.1	Image of an autoclave with pressure indicator which was used for melt infiltration under argon pressure	25
4.1	Pore size distribution of the metal oxide scaffolds	29
4.2	(a) XRD of $\text{NaNO}_2@\text{SBA-15}$ and $\text{NaNO}_2@\text{Al}_2\text{O}_3$ nanocomposites with different pore fillings (b) DRIFTS of $\text{NaNO}_2@\text{SBA-15}$ and $\text{NaNO}_2@\text{Al}_2\text{O}_3$ nanocomposites with different pore fillings	30
4.3	(a) Pore size distributions of SBA-15 and $\text{NaNO}_2@\text{SBA-15}$ nanocomposites (b) Pore size distribution of Al_2O_3 and $\text{NaNO}_2@\text{Al}_2\text{O}_3$ nanocomposites (c) Trends in remaining porosity of $\text{NaNO}_2@\text{SBA-15}$ and $\text{NaNO}_2@\text{Al}_2\text{O}_3$ nanocomposites	31
4.4	DSC of NaNO_2 , the $\text{NaNO}_2@\text{SBA-15}$ nanocomposite and the $\text{NaNO}_2@\text{Al}_2\text{O}_3$ nanocomposite	32
4.5	(a) XRD of both $\text{NaNO}_2@\text{Nb}_2\text{O}_5$ and $\text{NaNO}_3@\text{Nb}_2\text{O}_5$ nanocomposites (b) DRIFTS of both $\text{NaNO}_2@\text{Nb}_2\text{O}_5$ and $\text{NaNO}_3@\text{Nb}_2\text{O}_5$ nanocomposites	33
4.6	Conductivity of NaNO_2 and the $\text{NaNO}_2@\text{metaloxides}$ nanocomposites	34
4.7	Conductivity of NaNO_3 and the $\text{NaNO}_3@\text{metaloxides}$ nanocomposites	35
4.8	(a) Pyridine-FTIR spectrum of the metal oxide scaffolds at 150 °C (b) NH_3 -TPD spectra of the metal oxide scaffolds	35
4.9	(a) Conductivity of NaNO_2 before and after heat treatment (b) trends in conductivity of $\text{NaNO}_2@\text{Al}_2\text{O}_3$ nanocomposites with different pore fillings	37

4.10	Chemical structure of the model system with metallocene complexes grafted to the silica surface. Reprinted from Thornburg et al. ⁵⁸	39
4.11	Pore size distribution of some of the SiO ₂ scaffolds with metal atoms grafted on the surface	40
4.12	Conductivity of nanocomposites of NaNO ₂ and SiO ₂ scaffolds with metal atoms grafted on the surface	41
4.13	Conductivity of the nanocomposites of NaNO ₂ and SiO ₂ scaffolds with metal atoms grafted on the surface at 130 °C versus the ionic character of the M-O bond	41
6.1	(a) XRD of the NaNO ₂ @TiO ₂ nanocomposite (b) XRD of the NaNO ₂ @ZrO ₂ nanocomposite	56
6.2	XRD of the NaNO ₂ @Nb ₃ (PO ₄) ₅ and NaNO ₃ @Nb ₃ (PO ₄) ₅ nanocomposites	56
6.3	(a) DRIFTS of the NaNO ₂ @TiO ₂ nanocomposite (b) DRIFTS of the NaNO ₂ @ZrO ₂ nanocomposite	57
6.4	DRIFTS of the NaNO ₂ @Nb ₃ (PO ₄) ₅ and NaNO ₃ @Nb ₃ (PO ₄) ₅ nanocomposites	57
6.5	(a) DSC of the NaNO ₂ @TiO ₂ nanocomposite (b) DSC of the NaNO ₂ @ZrO ₂ nanocomposite	57
6.6	(a) DSC of the NaNO ₂ @Nb ₃ O ₅ nanocomposite (b) DSC of the NaNO ₂ @Nb ₃ (PO ₄) ₅ nanocomposite	58
6.7	XRD of NaNO ₂ @SiO ₂ -x nanocomposites	58
6.8	DRIFTS of NaNO ₂ @SiO ₂ -x nanocomposites	59
6.9	DSC of NaNO ₂ @SiO ₂ -x nanocomposites	59
6.10	(a) XRD of the NaNO ₃ @SBA-15 and NaNO ₃ @Al ₂ O ₃ nanocomposites (b) DRIFTS of the NaNO ₃ @SBA-15 and NaNO ₃ @Al ₂ O ₃ nanocomposites	60
6.11	(a) Pore size distribution of SBA-15 and NaNO ₃ @SBA-15 nanocomposites (b) Pore size distribution of Al ₂ O ₃ and NaNO ₃ @Al ₂ O ₃ nanocomposites	60
6.12	Trends in remaining porosity of NaNO ₃ @SBA-15 and NaNO ₃ @Al ₂ O ₃ nanocomposites of different pore fillings	60
6.13	DSC of the NaNO ₃ @SBA-15 and NaNO ₃ @Al ₂ O ₃ nanocomposites	61
6.14	(a) XRD of the NaNO ₃ @TiO ₂ nanocomposite (b) XRD of the NaNO ₃ @ZrO ₂ nanocomposite	61
6.15	(a) DRIFTS of the NaNO ₃ @TiO ₂ nanocomposite (b) DRIFTS of the NaNO ₃ @ZrO ₂ nanocomposite	61
6.16	(a) DSC of the NaNO ₃ @TiO ₂ nanocomposite (b) DSC of the NaNO ₃ @ZrO ₂ nanocomposite	62
6.17	(a) DSC of the NaNO ₃ @Nb ₃ O ₅ nanocomposite (b) DSC of the NaNO ₃ @Nb ₃ (PO ₄) ₅ nanocomposite	62

List of Tables

2.1	Characteristics of lithium and sodium. ^{7,16}	15
4.1	Pore volume and BET surface area of the metal oxide scaffolds	29
4.2	Onset melting temperature and melting enthalpy for NaNO ₂ , the NaNO ₂ @SBA-15 nanocomposite and the NaNO ₂ @Al ₂ O ₃ nanocomposite	32
4.3	Activation energies for ion hopping in NaNO ₂ and in the NaNO ₂ @metaloxides nanocomposites	34
4.4	Activation energies for the ion hopping in NaNO ₃ and in the NaNO ₃ @metaloxides nanocomposites	35
4.5	Summary of the results from Pyridine FTIR and NH ₃ TPD, giving the amount of acid sites and desorption temperatures of pyrdine and NH ₃	36
4.6	Porosity and surface area of some of the SiO ₂ scaffolds with metal atoms grafted on the surface	40
4.7	Activation energies for ion hopping in the nanocomposites of NaNO ₂ and SiO ₂ scaffolds with metal atoms grafted on the surface	41

List of Abbreviations

BET	Brunauer, Emmett and Teller
BJH	Barrett, Joyner and Halenda
DRIFTS	diffuse reflectance infrared Fourier transformed spectroscopy
DSC	differential scanning calorimetry
EIS	electrical impedance spectroscopy
FES	flywheel energy storage
FTIR spectroscopy	Fourier transformed infrared spectroscopy
IEA	International Energy Agency
LHS	latent heat storage
LIB	lithium ion battery
NASICON	Na super ionic conductor
NH₃-TPD	ammonia temperature programmed desorption
SBA-15	Santa Barbara Amorphous no. 15
SIB	sodium ion battery
SSE	solid-state electrolyte
STP	standard temperature and pressure
TEOS	tetraethyl orthosilicate
XRD	X-ray diffraction

1 Introduction

The International Energy Agency (IEA) stated in its annual report that the the global energy demand has increased with 2.3 % in 2018. Although the energy demand has been growing constantly over the past years, the current growth is the fastest within the last decade. This is the result of a robust global economy and the need for heating or cooling in some areas of the world. In addition, the report mentions that due to this increase in energy demand the emission of CO₂ rose with 1.7 % to a value of 33 Gigatonnes.¹ Since CO₂ is a greenhouse gas, it contributes to the global warming. In order not to exceed the value of 2 °C global warming agreed upon by the United Nations in Paris,² its emission should be limited. Therefore, a shift in energy sources from fossil fuels towards renewable energy sources is required. Although the energy from renewable energy sources increased by over 4 % in 2018, the IEA report clearly states that this is not enough to meet the climate goals.¹

Renewable energy sources, such as solar cells or windmills, have one important drawback making it hard to shift to renewable energy source: their energy supply is unpredictable and varying. Factors such as varying weather conditions and changing seasons influence the energy supply every single day. Changing from fossil fuels towards renewable energy sources requires energy storage systems to overcome the intermittent nature. These energy storage systems can store energy when the conditions are favourable and there is an excess of energy and they are able to release energy when the energy supply is insufficient. This is schematically depicted in figure 1.1.

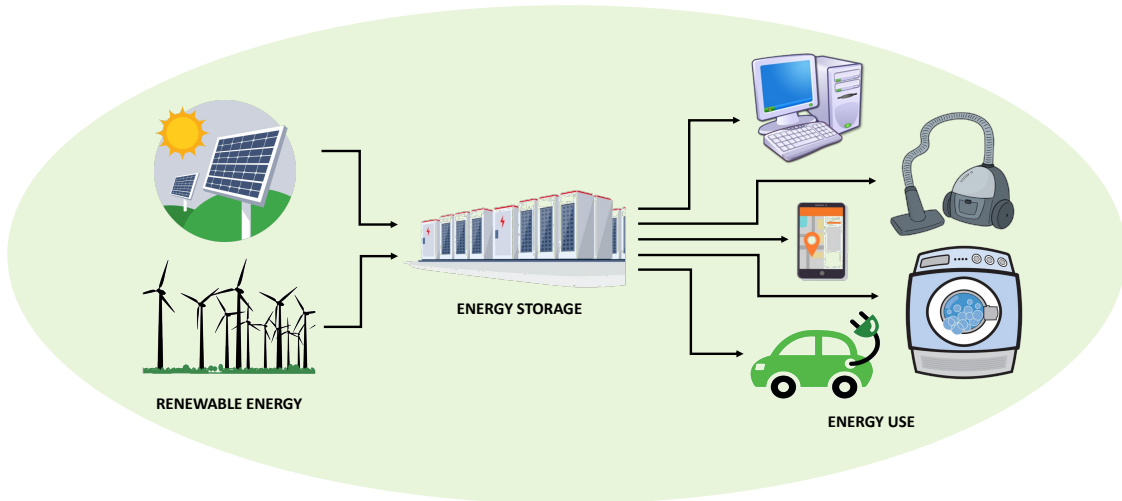


Figure 1.1: Schematic representation of the ideal energy grid, where energy is obtained from renewable energy sources, stored in energy storage systems to overcome the intermittent nature of renewable energy sources and finally supplied to the consumer.

Energy storage can be achieved in multiple ways: First of all, energy can be stored mechanically, for example flywheel energy storage (FES). In a FES, energy is stored by accelerating a rotor and maintaining the energy as rotational energy. Secondly, energy can be stored thermally. A good example of this is latent heat storage (LHS), where the heat absorption during a phase transition of the storage material is used to store energy. Thirdly, energy can be stored chemically. This particular method of energy storage has drawn much attention recently, since it has the potential of replacing petroleum products and reducing the greenhouse gas emission. Hydrogen energy storage is the most popular method of chemical energy storage. Here, energy is used to make hydrogen via electrolysis. However, safe and efficient storage of the hydrogen gas remains an important challenge. The last, but by no means least of energy storage is electrochemical energy storage, for example in batteries. In this case, energy is used to charge a battery by a chemical reaction leading to a potential difference between the two electrodes. Batteries are promising for energy storage, since they already find widespread application. Therefore, this work will focus on energy storage in batteries.³

Currently several types of rechargeable batteries exist, but the most often used battery is the lithium-ion battery (LIB). Given its excellent performance and wide scale applicability, the Nobel prize of 2019 was awarded to the inventors of this battery.⁴ However, LIBs are expensive due to the limited abundance of lithium.^{5,6} Hence, low-cost alternatives based on abundant metals, such as sodium, are developed.^{5,7-9} Sodium-ion batteries (SIBs) are attractive for large scale application, but there are still several challenges that need to be overcome. One of these challenges is the development of good electrolytes. Current SIBs operate at 300 °C due to a lack of proper electrolytes.^{8,10,11} A good electrolyte needs to meet several requirements, for example it needs to be safe, to have a high ion conductivity and to have a good interface with the electrodes.^{5,12} This thesis focusses on solving the challenge of finding good electrolytes by introducing a novel type of solid-state electrolytes based on low-cost salts such as sodium nitrites and sodium nitrates. These salts have low ion conductivities. Therefore, the goal of this thesis is to increase the ion conductivity by making nanocomposites of the sodium salts and metal oxide scaffolds and to study the effect of different scaffolds on the ion conductivity.

To understand the work performed, the thesis will start with a Theory chapter providing background information. The working of batteries will be explained, as well as challenges for current sodium ion batteries and the state of the art for research into sodium electrolytes. In the second part of this Theory chapter the necessary information in order to understand the synthesis and analysis methods used will be provided. Following this, the Experimental Method chapter will cover all the details and equipment setting used during the experiments. Next, the Results and Discussion chapter will deal with the results obtained. This chapter will be divided into two parts; the first part will describe the results of the synthesis and conductivity of nanocomposites of NaNO₂ and six different metal oxide scaffolds. The second part of the chapter will discuss the results of a model study to investigate the influence of acidity of surface groups on the conductivity. This thesis will end with summarizing all conclusions that can be drawn and indicating further prospects for the project.

2 Theory

In this chapter the theoretical background for this work will be provided. Part I will focus on the theory behind (sodium) batteries and sodium electrolytes. In Part II, the theory behind the most important synthesis and analysis techniques will be given.

2.1 Part I: Batteries

This part of the Theory chapter will give a short introduction into batteries and especially sodium batteries. The most important challenges to improve sodium-ion batteries will be discussed, leading to a focus on developing novel electrolytes.

2.1.1 Introduction to batteries

Different types of rechargeable batteries exist, among which are lead-acid, nickel-cadmium, nickel-metal hydride, and lithium-ion batteries. These days, the lithium-ion battery (LIB) is the most widely used rechargeable battery and the inventors, John Goodenough, Stanley Whittingham, and Akira Yoshino, were awarded the Nobel Prize of Chemistry in 2019. The working principles of a rechargeable battery will be explained using this battery, which is schematically depicted in figure 2.1. A battery consists of two electrodes, an anode and a cathode, with an electrolyte in between. The working principle is based on redox reactions due to a potential difference between the cathode and the anode. Normally, the anode and cathode are not electronically connected and nothing happens. In the discharged mode, the anode is electronically connected to the cathode via an electronic circuit. Therefore, the anode is oxidized and electrons flow through the circuit to the cathode, which is reduced. To maintain charge neutrality, positive ions move from the anode through the electrolyte to the cathode. During charging this process is reversed.⁴ The LIB uses intercalated materials for the electrodes: the anode is made

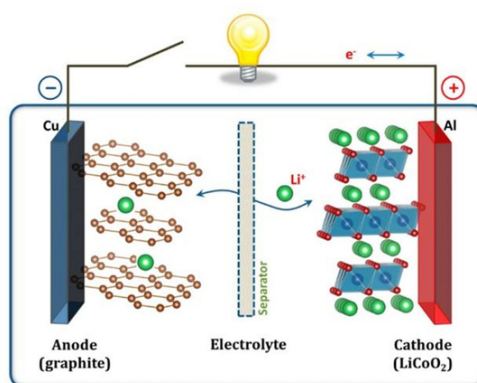
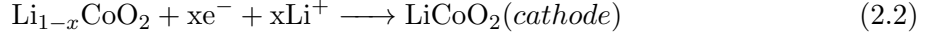
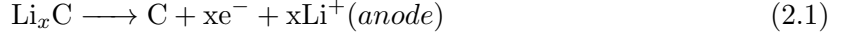


Figure 2.1: Schematic representation of the first Li-ion battery (LiCoO₂ cathode, Li⁺ electrolyte and graphite anode). Reprinted from Goodenough et al.¹³

of metallic lithium intercalated in graphene, Li_xC , and the cathode of Li_xCoO_2 , an intercalated metal chalcogenide. Lithium salts like LiPF_6 in organic liquids are used as electrolyte. The following half reactions take place at the anode and cathode upon discharging:



Combined, these two half reaction lead to the following overall reaction with a potential difference of $\sim 4\text{ V}$:¹³



Despite their widespread application, LIBs also have some disadvantages. First of all, the energy density is limited due to the use of intercalated materials as electrodes. Intercalated electrodes are used since pure electrodes, especially pure metallic anodes, react with the electrolyte. Furthermore, the use of organic liquids in the electrolytes causes safety risks associated with the flammability and volatility of the solvents.¹⁴ These problems can be overcome by improving the current battery and in particular by improving the electrolyte. Solid-state electrolytes (SSE) are promising to overcome these problems and research has led to several classes of solid-state electrolytes.

However, there is another disadvantage that cannot be easily overcome: lithium is a relatively scarce metal. Some authors claim that the current lithium resources can only sustain for 65 years.^{5,6} Although this statement is under debate, it is clear that LIBs will be costly and therefore less suited for large scale applications, such as grid-scale energy storage. Therefore, low-cost alternatives have investigated and sodium-ion batteries (SIBs) seem to be a promising alternative.^{5,7-9}

2.1.2 Sodium batteries

Sodium is investigated as an alternative for LIBs, since sodium is in the same main group of the periodic table, hence demonstrating similar electrochemical properties as lithium.¹⁵ Table 2.1 shows some characteristics of lithium and sodium.^{7,16} This table shows that sodium is clearly cheaper than lithium and it has a redox potential suitable for application in batteries. However, the table shows also that the energy density of sodium is significantly lower than that of lithium. Nevertheless, SIBs are better than LIBs in terms of price per kW energy per gram material. Therefore, applications of SIBs will be limited to static applications as energy storage, whereas applications of LIBs will be for portable/moving applications like smartphones, laptops and electric vehicles.⁸ In general, SIBs are in a less developed state than LIBs. Given the chemical similarities of lithium and sodium, much of the sodium research is based on copying experiments that turned out successful for lithium. Talking about the research on sodium batteries, it might be useful to discuss the current state of the art for SIBs and research into SIBs.

Characteristic	Na	Li
Cation radius	0.97 Å	0.69 Å
Capacity metal	1.16 Ahg ⁻¹	3.86 Ahg ⁻¹
Voltage <i>vs</i> SHE	-2.7 V	-3.0 V
Melting point	97.7 °C	180.5 °C
Price (carbonates)	0.07-0.37 €kg ⁻¹	4.11-4.49 €kg ⁻¹

Table 2.1: Characteristics of lithium and sodium.^{7,16}

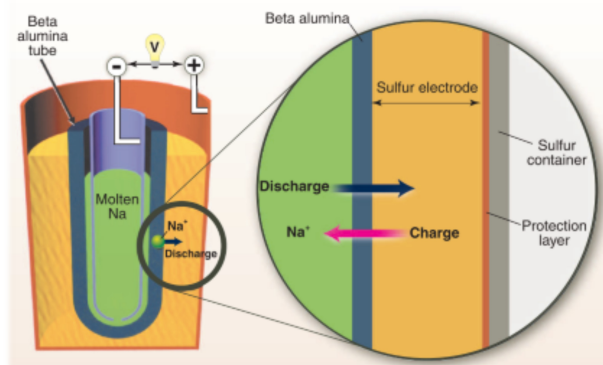


Figure 2.2: Schematic representation of a NaS battery with a molten Na anode, a S cathode and sodium β -alumina electrolyte. Reprinted from Dunn et al.¹⁰

These days, NaS and NaNiCl_2 solid state batteries (SSB) are commercially available. The development of SIBs started from the the 1960s when researchers at Ford discovered that sodium β -alumina ($\text{NaAl}_{11}\text{O}_{17}$) exhibits conductivity for sodium ions at elevated temperatures (300 °C to 350 °C).¹⁷ This electrolyte was used to make a NaS battery, which is schematically depicted in figure 2.2. The working temperature of this battery is 300 °C to 350 °C, not only to obtain a high ionic conductivity in the electrolyte, but also to ensure the electrodes are molten, allowing them to have a good contact at the interface with the electrolyte.^{8,10} In the early 1980s the NaNiCl_2 battery was developed, and was given the nickname ZEBRA battery (both based on its scientific origin in Africa and the acronym Zero-Emission Battery Research Activities). This battery operates between 300 °C to 350 °C as well and uses molten Na as anode, molten NiCl_2 as cathode and molten NaAlCl_4 in β -alumina as electrolyte.^{10,11} An important disadvantage of these SIBs is their operating temperature, needed for the electrolyte to be conductive. Therefore, a substantial amount of research is done on sodium electrolytes that conduct ions at room temperature. The next section covers this topic of research on sodium based electrolytes.

2.1.3 Sodium electrolytes

In an ideal case an electrolyte is found with the following properties: 1) a high ionic conductivity (Na^+ conductivity of $\gtrsim 10^{-3} \text{ Scm}^{-1}$ at room temperature) 2) a good interfacial contact with the electrodes 3) chemically stable, 4) electrochemically stable 5) thermally stable 6) low toxicity and 7) low costs.^{5,12} Currently, different types of sodium electrolytes are being investigated. Unfortunately, none of them meets all these requirements.

A logical first step to design a good electrolyte is to take the current LIB electrolyte as a 'blue print' and use sodium salt like NaPF_6 and NaClO_4 in organic liquids.^{5,16,18} For NaPF_6 in propylene carbonate a conductivity of $7.98 \times 10^{-3} \text{ Scm}^{-1}$ at room temperature was found.¹⁹ The main disadvantage of these electrolytes is the flammability of the organic liquid leading to safety issues.

Another type of sodium electrolytes are polymer electrolytes. Both gel polymer containing a solvent and solvent-free polymer electrolytes exist.⁹ The basic idea of gel polymer electrolytes is that the salt solution is retained in the polymeric gel. The salt solution provides the ion conductivity, whilst the polymer enhances the mechanical stability.⁷ Ions other than Na ions can contribute to the ion conductivity as well. Polyvinylidene fluoride is often used as polymer matrix and for these electrolytes conductivities in the order of 10^{-3} Scm^{-1} at room temperature were found.^{9,20,21} However, gel polymers do not solve the problem of the presence of flammable and volatile liquids. Solid-state electrolytes (SSE) can overcome this problem. Different types

of SSEs exist. A first type of SSEs are solvent-free polymer electrolytes. In these electrolytes sodium salts are dissolved by the polymer chain and the ion conduction is based on the ion hopping along the polymer chain. The increase in safety of not using solvents is at the expense of ion conductivity: solvent-free polymers have conductivities lower than 10^{-5} Scm^{-1} at room temperature.^{9,22}

Another promising SSE is the NASICON (NA Super Ion CONductor) electrolyte, which was discovered in the 1970s by Goodenough and Hong. They described the NASICON compound as a solid solution of $\text{NaZr}_2\text{P}_3\text{O}_{12}$ and $\text{Na}_4\text{Zr}_2\text{Si}_3\text{O}_{12}$ with the chemical formula $\text{Na}_{1+x}\text{Zr}_2\text{S}_x\text{P}_{3-x}\text{O}_{12}$ and $0 \leq x \leq 3$. Their compounds had an ion conductivity of 0.2 Scm^{-1} at 300°C .^{23,24} Nowadays, the name NASICON is used for compounds with the formula $\text{AMP}_3\text{O}_{12}$, where A can be a monovalent, divalent, trivalent or tetravalent cation and M a divalent, trivalent tetravalent or pentavalent cation. Electrolytes then consist of a $\text{NaAMP}_3\text{O}_{12}$ ion conductor and conductivities up to $2.7 \times 10^{-3} \text{ Scm}^{-1}$ at room temperature were found.^{9,25} Nevertheless, these materials cannot be applied yet, since they have a poor contact with the electrodes and dendrites are formed at the boundaries of the electrolyte.

Given the high conductivity of complex lithium hydrides, the conductivity of complex sodium hydrides were investigated as well. These electrolytes are solid-state electrolytes too. Different complex sodium hydrides are investigated, amongst others $\text{Na}_2(\text{BH}_4)(\text{NH}_2)$, $\text{Na}_2\text{B}_{12}\text{H}_{12}$, $\text{Na}_2\text{B}_{10}\text{H}_{10}$, NaAlH_4 and Na_3AlH_6 .^{14,26–30} These salts showed conductivities of respectively $2 \times 10^{-6} \text{ Scm}^{-1}$ at room temperature, 0.1 Scm^{-1} above 250°C , 0.01 Scm^{-1} at 110°C , $2.1 \times 10^{-10} \text{ Scm}^{-1}$ at room temperature and $4.1 \times 10^{-4} \text{ Scm}^{-1}$ at 160°C . Our research group has investigated confinement of complex metal hydrides into porous scaffolds via melt infiltration for lithium and sodium. Confinement of lithium borohydride can increase the conductivity up to $1 \times 10^{-4} \text{ Scm}^{-1}$ at room temperature³¹ and confinement of sodium borohydride can increase the conductivity up to $2.7 \times 10^{-6} \text{ Scm}^{-1}$ at room temperature.³² The biggest disadvantage of these nanocomposites is their stability, since they react with air and water. For the NaBH_4 based nanocomposites there is no literature explaining the increased conductivity, but for LiBH_4 based nanocomposites it is known that the increased conductivity is caused by interfacial effects.^{31,33–35} For nanocomposites of LiBH_4 and SiO_2 prepared via melt infiltration it is shown that a fraction of the confined LiBH_4 located close to the SiO_2 surface forms a different phase than the rest of the confined LiBH_4 . This phase is highly conductive. Similar results were found for nanocomposites of LiBH_4 and both SiO_2 and Al_2O_3 prepared via ball milling.^{33,34} On top of that, for nanocomposites of LiBH_4 and SiO_2 prepared via melt infiltration, it was proven that the amount of hydroxyl group on the SiO_2 surface influences the conductivity. These results on LiBH_4 based nanocomposites provide a basis for further rational design of solid-state nanocomposites via interface engineering. Therefore, this work investigates whether nanoconfinement can also increase the conductivity of stable salts as NaNO_2 and NaNO_3 and which factors influence that process. NaNO_2 and NaNO_3 are investigated, since they have low melting points (respectively 271°C and 308°C), which is beneficial for a good electrode-electrolyte interface. Besides, they are stable in air, since the salt can be stored in air. There is no literature available for the electrochemical stability of NaNO_2 and NaNO_3 . Although no information is available on the electrochemical stability of the sodium salts, the lithium analogue, LiNO_3 , is often used as an electrolyte additive with a stability of $\sim 2 \text{ V}$ and it is even known for increasing the stability of liquid electrolytes.^{36–38}

2.2 Part II: Methods

This part of the Theory chapter will outline the concepts behind the synthesis of the nanocomposites and the analysis techniques used. There will be briefly mentioned for each analysis technique what it measures and what information the technique gives.

2.2.1 Synthesis: Melt Infiltration

The nanocomposites investigated in this work are synthesized by melt infiltration of sodium salts, NaNO_2 and NaNO_3 , in the pores of metal oxide scaffolds. Melt infiltration is a process where liquids (the molten salts) are drawn into the pores of a template (the scaffold) by capillary forces. De Jongh et al.³⁹ explained how melt infiltration is determined by wetting, capillarity and viscous flow. Wetting of a liquid droplet on a solid surface (figure 2.3) depends on the surface energies of the solid and the liquid. Young's equation (equation 2.4) gives the relation between the surface energy of the solid (γ_{sv}), the liquid (γ_{lv}) and the solid-liquid interface (γ_{sl}):

$$\cos\theta_c = \frac{\gamma_{sv} - \gamma_{sl}}{\gamma_{lv}} \quad (2.4)$$

For a contact angle $\theta_c > 90^\circ$, there is wetting, whilst for a contact angle $\theta_c < 90^\circ$ the system does not wet. Typical surface energies for amorphous silica and γ -alumina are respectively 0.3 Jm^{-2} and 1.5 Jm^{-2} .^{40,41} For NaNO_2 and NaNO_3 their surface tensions are respectively 0.12 Jm^{-2} and 0.12 Jm^{-2} at their melting points.⁴² The surface tensions of the molten salts decrease upon heating. In case of wetting, the capillaries (the pores of the scaffold) fill automatically, since this leads to favourable interactions between the liquid and the wall. The rate of infiltration depends on the pore radius, the wetting behaviour and the viscosity of the liquid. The higher the viscosity of the liquid, the slower it infiltrates.

2.2.2 Analysis

The pure salts, bare scaffolds and synthesized nanocomposites were analysed using X-ray diffraction (XRD), diffuse reflectance infrared spectroscopy (DRIFTS), differential scanning calorimetry (DSC), nitrogen physisorption (N_2 -physisorption), pyridine-Fourier transformed infrared spectroscopy (pyridine-FTIR), ammonia temperature programmed desorption (NH_3 -TPD) and electrochemical impedance spectroscopy (EIS). Therefore, these techniques are explained in more detail.

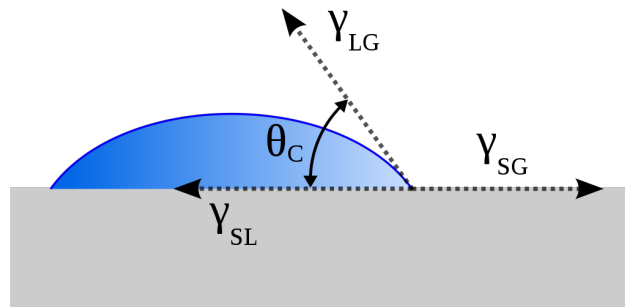


Figure 2.3: Schematic representation of a liquid droplet wetting a solid surface, with γ_{sv} the surface energy of the solid, γ_{lv} the surface energy of the liquid, γ_{sl} the surface energy of solid-liquid interface and $\theta_c >$ the contact angle.

2.2.2.1 Nitrogen Physisorption (N₂-physisorption)

Physisorption is a method to obtain information about the porosity, pore size distribution and surface area of a sample. It will be used to determine these parameters for the scaffolds to know what materials are started with. It will be measured for some of the nanocomposites as well, since the remaining porosity can indicate whether melt infiltration was successful or not. Physisorption measures adsorption of a gas (N₂) on the surface of a material. N₂-physisorption is typically performed at 77 K, the boiling point of nitrogen. In a typical physisorption experiment, the sample is degassed to vacuum. Then, specific amounts of gas are added to the sample. The volume of gas absorbed can be determined by comparing the amount of gas added with the relative nitrogen pressure (defined as p/p_0 , where p and p_0 are respectively the equilibrium pressure and the relative saturation pressure). Since the experiment is performed at low temperatures and low pressure, the value for the adsorbed volume need to be converted to a value at standard temperature and pressure (STP). By plotting the converted adsorbed volume versus the relative nitrogen pressure for different amounts of nitrogen added an adsorption isotherm can be obtained. Desorption isotherms can be obtained by reversing the experiment and plotting the data. The total pore volume of the sample is the absorbed volume at a relative pressure of $p/p_0 \approx 1$.⁴³ Barrett, Joyner and Halenda (BJH) provided an analysis to extract the pore size distribution from the isotherm and Brunauer-Emmett-Teller (BET) describe a theory to obtain the surface area.^{44,45}

2.2.2.2 X-ray Diffraction (XRD)

Using X-ray diffraction information about amongst others the presence of crystalline phases can be obtained. Bulk material of NaNO₂ and NaNO₃ is crystalline. XRD spectra of the nanocomposites can indicate whether the sodium salt is still presents as bulk phase, or whether it has reacted or formed an amorphous phase. In a XRD experiment a beam of X-rays is sent through a sample, where atoms will scatter the electromagnetic waves. In case of a crystalline sample, the scattered x-rays have constructive interference for specific angles of the incoming beam depending on the lattice spacing, which is shown in figure 2.4. The relation between the angle of the incoming beam and the lattice spacing for constructive interference is given by Bragg's law (equation 2.5):

$$n\lambda = 2d\sin\theta \quad (2.5)$$

where n is the order of the reflection and can be any integer value, λ is the wavelength of the X-rays, d is the lattice spacing and θ is the incident angle. In a XRD graph, the intensity of the diffraction peaks is plotted versus twice the incident angle.

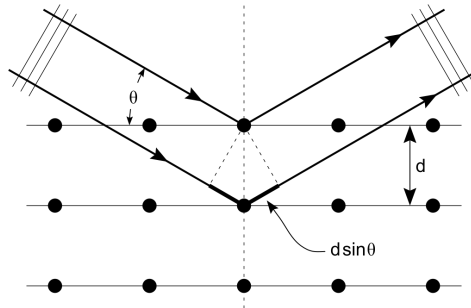


Figure 2.4: Schematic representation of X-ray diffraction. The X-ray beam (incident angle θ) is diffracted by the crystalline material with lattice spacing d .

2.2.2.3 Diffuse Reflectance Infrared Fourier Transform (DRIFTS)

Diffuse reflectance infrared Fourier transform spectroscopy provides information about molecular bond vibrations. The vibration of the NO_2^- and NO_3^- anions and in particular the vibrations of groups on the surface of the scaffolds are of interest. The former can give information on whether the salt is still presents or whether it has reacted. At the same time, quenching of surface group vibrations is a indication for interactions between the scaffold and the sodium salt and thus an indication for successful melt infiltration. In a DRIFT experiment the sample is illuminated with infrared light. The infrared light can be scattered directly, or first interact with the sample and then scatter diffusely. The direct scattered light is often lost; the diffusely scattered light is collected with a mirror. Molecular bonds can absorb the infrared light to excite their vibrations. By comparing the diffused infrared light with the original beam these absorptions can be found. In a DRIFTS graph the absorption intensity is plotted versus the wavelength of the infrared light.

2.2.2.4 Differential Scanning Calorimetry (DSC)

With differential scanning calorimetry (DSC) information about phase transition can be obtained. NaNO_2 has two phase transitions: a first transition around 163°C , where ferroelectric NaNO_2 crystals transform into a antiferroelectric phase and a second transition due to the melting at 271°C .⁴⁶ NaNO_3 has two phase transitions too: around 276°C the lattice expands and at 308°C the salt melts.^{47,48} For the nanocomposites it is interesting to look at the changes in the melting peak of NaNO_2 or NaNO_3 . Several changes are possible. First of all, interactions between the sodium salt and the scaffold can slightly change the melting point. Secondly, nanoconfinement lowers the melting point. Therefore, it is expected to find an additional melting peak next to the bulk peak for melting of the salt that is confined in the pores. Thirdly, peaks can disappear or new peaks can appear, if the salt reacts and new compounds are formed. So, DSC can give a good indication whether melt infiltration was successful or not. In a DSC experiment a sample and a reference are maintained at the same, changing temperature. By comparing the heat flow needed to arrive at a certain temperature for the sample and the reference, phase transitions can be found. In a DSC graph, the heat flow is plotted versus the temperature. Endothermic phase transitions need extra heat flow and therefore lead to negative peaks. Exothermic phase transitions produce heat and therefore lead to positive peaks.

2.2.2.5 Pyridine Fourier Transformed Infrared Spectroscopy (pyridine-FTIR)

Pyridine Fourier transformed infrared spectroscopy is a method to investigate the presence of Lewis and Brønsted acidity on the surface of a sample. In this work the acid sites on the surface of the metal oxide scaffolds will be determined. These sites can interact with other materials containing Lewis or Brønsted bases, e.g. the anions of the sodium salts, changing properties such as the ion conductivity of the salt. In pyridine-FTIR, pyridine is used as a probe molecule. The lone pair of the nitrogen can coordinate to a Lewis acid site. Besides, it can form a hydrogen bond with Brønsted acid sites or it can be protonated by a Brønsted acid site. These interactions are depicted in figure 2.5. These interactions can be followed with Fourier transformed infrared spectroscopy (FTIR), since the interactions lead to specific molecular vibrations of the pyridine molecule. Brønsted acid sites give peaks around 1545 cm^{-1} . The intensity of the peak provides information on the number of Brønsted acid sites present. The exact position gives information on the strength of the acid site. The stronger the acid site, the higher the wavelength of the vibration. Lewis acid sites give rise to a peak around 1450 cm^{-1} and a peak between $1600 - 1630\text{ cm}^{-1}$. Integration of the former gives the amount of acid sites and the position of the later

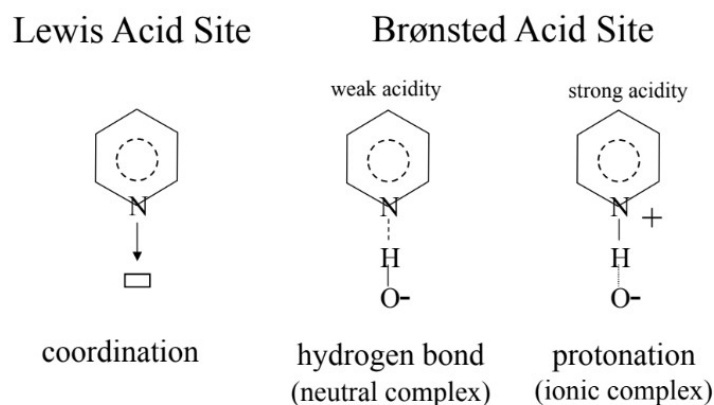


Figure 2.5: Interactions of pyridine with Lewis and Brønsted acid sites

determines the strength of the Lewis acidity. Both Lewis and Brønsted acidity give rise to a peak around 1490 cm^{-1} . Since it does not differentiate between Lewis and Brønsted acidity, the peak is not used in analysis.^{49,50}

In a typical Pyridine-FTIR experiment, pyridine first absorbs to a dried sample under vacuum. Then the sample is heated a little to remove physisorbed pyridine. Thereafter, the sample is heated further to desorb the pyridine. The desorption temperature of pyridine is a measure for the strength of the acid sites. During this whole process FTIR spectra are taken, to follow the adsorption and desorption of pyridine. In general, a pyridine-FTIR measurement underestimates the acidity.⁵¹

2.2.3 Ammonia temperature programmed desorption(NH₃-TPD)

Ammonia temperature programmed desorption (NH₃-TPD) is another method to determine the acid sites on a scaffold. It will be used to confirm the results from pyridine-FTIR for the metal oxide scaffolds. In this case, ammonia is used as a probe molecule. Ammonia has some practical advantages compared to pyridine. It is easier to handle, since it is a gas, it is less toxic than pyridine and due to its smaller size it can also probe acidity in small pores.⁵² NH₃-TPD does not differentiate between Lewis and Brønsted acid sites and overestimates the acidity in general. In a NH₃-TPD measurement, first the sample is dried under heating. Then, a pulse of NH₃ is given and the NH₃ chemisorbs to the surface. Subsequently, the sample is heated and the amount of NH₃ that desorbs from the sample is measured and plotted versus the temperature. If the sample has acid sites, these graphs show peaks. The position of the peak gives information on the strength of the acid site. The stronger the acid site, the higher the desorption temperature. Furthermore, the amount of acid sites can be determined via integration of the peaks.

2.2.4 Electrochemical Impedance Spectroscopy (EIS)

Electrochemical Impedance Spectroscopy can be used to determine amongst others the conductivity of a sample. In this work it will be used to determine the conductivity of the nanocomposites. Since this measurement will form a key element of the research performed in this work, the analysis will be explained in more depth, using the lecture notes from B. Ern  from the Colloid Science course.⁵³ The easiest way to measure the conductivity of a compound is determining the resistance by measuring the current at a certain voltage. Ohm's law (equation 2.6) shows

how the resistance is related to the applied voltage and current:

$$V = IR \quad (2.6)$$

where V is the applied voltage, I the current and R the resistance. The conductivity is then inversely proportional to the resistance:

$$\sigma = \frac{A}{dR} \quad (2.7)$$

where A is the area, d the distance and σ the conductivity. However, this method does not work for electrolytes. As electrolytes consist of positive and negative ions, the ions will form electrical double layers at the surface of the electrodes. These electrical double layers behave as condensators. Therefore, the electrolyte is often represented as a condensator, a resistor and again a condensator in series, instead of just a resistor. The double layers are not simple solid-state condensators, as they consist of ions that move back into the solution depending on the concentration of ions in the double layer. This makes it hard to determine the resistance of the electrolyte. In theory it is possible to measure the resistance before the electrical double layers are formed. In practise however, this is hard, as the double layers form quickly. Therefore, conductivity of electrolytes is often measured using alternating potentials, preventing double layers to form. In a system with alternating voltage and alternating current, the ratio between these two is the electrical impedance:

$$Z = \frac{\tilde{V}}{\tilde{I}} \quad (2.8)$$

with Z the electrical impedance, \tilde{V} the applied alternating voltage and \tilde{I} alternating current. In a EIS measurement the alternating current is measured. The conductivity can be derived from the impedance. The impedance is a combination of several facets: the resistance of the electrolyte, the cell capacitance, the impedance of the electrical double layers at the surface of the electrodes and the impedance of connecting cables. When sufficiently high frequencies are applied, the electrical double layer formation is negligible and the system can be considered as an resistor (due to the electrolyte resistance) and a capacitor connected in parallel. For the resistor, the voltage and the current have the same phase, so the impedance of the resistor is equal to de resistance:

$$Z_R = \frac{V \sin(\omega t)}{I \sin(\omega t)} = R \quad (2.9)$$

For the condensator, the current and the voltage do not have the same phase and the impedance of the condensator is given by:

$$Z_C = \frac{\tilde{V}}{\tilde{I}} = \frac{V \sin(\omega t)}{C\omega V \sin(\omega t + 1/2\pi)} = \frac{1}{j\omega C} \quad (2.10)$$

Then, the impedance of the whole system can be given by:

$$Z = \frac{1}{\frac{1}{Z_R} + \frac{1}{Z_C}} = \frac{1}{\frac{1}{R} + j\omega C} \quad (2.11)$$

This can be rewritten into a real component and an imaginary component:

$$Z = \frac{R}{1 + (\omega RC)^2} - j \frac{\omega R^2 C}{1 + (\omega RC)^2} \quad (2.12)$$

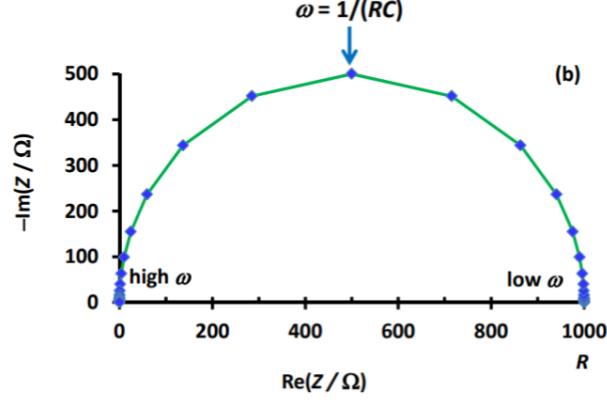


Figure 2.6: Nyquist plot: plot of the imaginary part of the impedance versus the real part. The non-zero intersection with the x-axis give the resistance R . Reprinted from Ern .⁵³

The real and imaginary part can be used to obtain the resistance. Typically, EIS data is presented in a so-called Nyquist plot, where the imaginary part is plotted versus the real part for each data point. In an ideal scenario, these data points form a semicircle. The non-zero intersection of the semicircle with the x-axis gives the resistance of the sample measured. A Nyquist plot and the intersection with the x-axis are given in figure 2.6. Using equation 2.7 the conductivity can be calculated. The conductivity is often measured at different temperatures. Plotting the conductivities on a logarithmic scale versus the inverse temperature leads to an Arrhenius-type behaviour, if the sample is conductive. The activation energy for ion hopping can be calculated using the slope of the conductivity plot and the Arrhenius equation, given in equation 2.13:

$$\sigma = Ae^{-E_{Act}/k_B T} \quad (2.13)$$

where σ is the conductivity, E_{Act} the activation energy for ion hopping, k_B the Boltzmann constant and T the temperature.

3 Experimental Method

This chapter will provide the experimental details of the practical work performed. First, specifications of the chemicals used and the synthesis performed will be given. Then, specifications of the analysis techniques will be discussed.

3.1 Synthesis

3.1.1 Scaffolds

In this work SBA-15 (SiO_2), Al_2O_3 , TiO_2 , Nb_2O_5 , $\text{Nb}_3(\text{PO}_4)_5$, ZrO_2 and SiO_2 with different metal atoms (Hf, Ti, Zr, Mo, Nb, Ta and Ba) grafted onto the surface were used as scaffold. The Al_2O_3 (γ - Al_2O_3 , Puralox SCCa-5/200), TiO_2 (Aeroxide P90, Evonik), Nb_2O_5 (Companhia Brasileira de Metalurgia e Mineração (CBMM), HY-340, AD/4465), $\text{Nb}_3(\text{PO}_4)_5$ (CBMM, AD/210) and ZrO_2 (Gimex technische keramiek b.v.) were commercially available. They were dried and stored in an Argon glovebox ($\text{H}_2\text{O} < 0.1$ ppm and $\text{O}_2 < 0.1$ ppm). Al_2O_3 was dried under N_2 -flow at 200°C for 3 h, the other scaffolds were dried under vacuum at 200°C for more than 20 h.

SBA-15 was synthesized using a method based on Lee et al.⁵⁴ Pluronic P123 ($\text{EO}_{20}\text{PO}_{70}\text{EO}_{20}$, average $M_W = 5800$, Aldrich) was dissolved in a mixture of deionized water and HCl (37 %, fuming, Emsure, analysis grade) in a polypropylene bottle and stirred vigorously for at least 3 h at 55°C (oil bath temperature). Then, tetraethyl orthosilicate (TEOS, $> 99.0\%$, Aldrich) was added under controlled stirring. The weight ratio of Pluronic P123, deionized water, HCL and TEOS was 1:26:6:2. After 2 min the stirring bar was removed from the reaction mixture and the lid of the bottle was closed tightly. The mixture was kept at 55°C for 24 h. Then, the SBA-15 was condensed further at 90°C for 24 h. Thereafter, SBA-15 was filtrated and washed with deionized water using a Buchner funnel until the pH of the filtrate was comparable to deionized water. The residue was dried at 60°C for 2-3 days and crushed into a fine powder afterwards. Then it was calcined at 550°C for 6 h (heating ramp $< 1^\circ\text{C}/\text{min}$). After calcination, the SBA-15 was dried under vacuum at 120°C for more than 20 h and stored in the glovebox ($\text{H}_2\text{O} < 0.1$ ppm and $\text{O}_2 < 0.1$ ppm).

For the synthesis of the metallocene grafted onto SiO_2 scaffolds a method adapted from literature was used.^{55,56} The silica (GRACE SI1404) was dried under vacuum at 220°C . Then, it was dispersed in 20 mL anhydrous 1,2-dichloroethane under a N_2 -atmosphere. Thereafter, a solution of the metallocene dissolved in a 1,2-dichloroethane was added. To allow diffusion of the metallocene into the pores, the mixture was stirred at 60°C for 1 h. Thereafter, 2.0 mL of anhydrous triethylamine was added at room temperature and the mixture was heated at 60°C for 3 h. Then, the mixture was filtrated to recover the grafted scaffolds. The scaffolds were washed 3 times with plenty of anhydrous chloroform. Subsequently, it was first dried in vacuo and then calcined in static air at 500°C for 4 h (ramp $10^\circ\text{C}/\text{min}$). The functionalized silicas were dried under vacuum at 150°C for more than 20 h and were stored in the glovebox ($\text{H}_2\text{O} < 0.1$ ppm and $\text{O}_2 < 0.1$ ppm).

3.1.2 Melt Infiltration

Melt infiltration was used to make the nanocomposites. For melt infiltration, NaNO_2 (both Acros Organics and 99.999 %, Aldrich) and/or NaNO_3 (> 99.0 %, Honeywell) were melt infiltrated in the scaffolds mentioned in the previous section. Both salts were dried at 150 °C or higher for 20 h and brought in the glovebox before melt infiltration. Melt infiltration samples were prepared in the glovebox and the mixtures were thoroughly crushed with pestle and mortar. The amount of sodium salt and scaffold in the mixture were chosen in such a way that the volume of the salt corresponded to a certain percentage of the pore volume of the scaffold. This approach was used, because it is known that the amount of the pore volume filled (the pore filling) influences the conductivity of the nanocomposites.³² The pore filling was based on the pore volume determined with N_2 -physisorption. After crushing, the mixtures were transferred into glass reactors that were placed in an autoclave. The autoclave is equipped with a pressure indicator and was held air tight by an Teflon O-ring. Figure 3.1 shows an image of the autoclave used. All melt infiltrations were performed under 30 bar argon pressure. For the melt infiltration, the autoclave was heated to 300 °C with a heating ramp of 3.2 °C/min. Then, the temperature was held at 300 °C for 30 min. Subsequently, the autoclave cooled down to room temperature. Finally, the excess pressure was removed and the autoclave was brought back in the glovebox (H_2O < 0.1 ppm and O_2 < 0.1 ppm), where the samples were stored.



Figure 3.1: Image of an autoclave with pressure indicator which was used for melt infiltration under argon pressure

3.2 Analysis

The bare scaffolds, salts and nanocomposites were characterized with N_2 -physisorption, XRD, DRIFTS, DSC, pyridine-FTIR and NH_3 -TPD. The conductivity was determined using EIS. Therefore, the specifications and settings of these techniques will be given in this section.

3.2.1 N_2 -physisorption

Nitrogen physisorption was measured with two set-ups: a Micromeritics TriStar 3000 and a Micromeritics TriStar II Plus. Measurements were performed by liquid N_2 at 77 K. Since the samples were dried before (see section Scaffolds) and stored in the glovebox, there was no need

for a drying step. The samples were prepared in the glovebox and brought outside shortly before the measurement. The BET method was used to determine the surface area⁴⁴ and the BJH analysis was performed to determine the pore size distribution.⁴⁵ The total pore volume of the sample is the absorbed volume at a relative pressure of $p/p_0 \approx 1$.

3.2.2 XRD

X-Ray diffraction patterns were obtained with a Bruker-AXS Advance power X-ray diffractometer, using a Cobalt $K_{\alpha 1,2}$ ($\lambda = 1.79026 \text{ \AA}$) source operating at 30 kV and 40 mA or 45 mA. Typical measurements were performed from 26° to 81° with a step size between 0.03° - 0.05° $2\theta^\circ$ and a scan speed of 1.0 s. The samples were prepared in the glovebox in a customized Bruker airtight specimen holder to keep the sample in an argon atmosphere.

3.2.3 DRIFTS

DRIFT spectra were measured on a Perkin Elmer IR with a MCT detector cooled by liquid nitrogen. Infrared spectra were collected between 4500 cm^{-1} and 400 cm^{-1} . The spectra were collected in absorption units, with a resolution of 4 cm^{-1} and they were averaged over 16 scans. Before measuring, the background was measured using KBr powder. The samples were prepared in the glovebox by filling a $40 \text{ }\mu\text{l}$ aluminium hermetic TGA sample holder from Perkin Elmer with sample. A home-build airtight sample holder was used to perform the measurement under inert atmosphere.

3.2.4 DSC

DSC measurements were performed using a Mettler Toledo HP DSC1. The data was recorded while heating and cooling the sample between 30°C and 320°C with a ramp of $5^\circ\text{C}/\text{min}$. Measurements were performed under a argon pressure and flow of 2 bar and $10 \text{ mL}/\text{min}$. Each measurement was repeated 2 times to check the reproducibility. The samples were prepared in the glovebox. Between 5 mg and 10 mg was measured exact in a $40 \text{ }\mu\text{l}$ aluminium hermetic TGA sample holder from Perkin Elmer. The STAR software was used to process the thermograms and determine the integrals of the phase transition peaks.

3.2.5 pyridine-FTIR

Pyridine-FTIR was measured by taking FTIR spectra after pyridine adsorption. The FTIR spectra were performed on a Perkin Elmer System 2000 with a DTGS detector. The spectra were collected in absorption units with a resolution of 4 cm^{-1} and they were averaged over 16 scans. A background scan was measured under vacuum. The sample was prepared in the glovebox by pressing a self-supporting pellet (7 mm diameter). The obtained sample was placed in the measurement cell inside the glovebox and subsequently brought outside the glovebox. Outside the glovebox, the measurement cell was connected to the set-up and the system was put under vacuum. Then, pyridine vapors ($\sim 22 \text{ bar}$) were allowed in the measurement cell. The system was equilibrated for 30 min. Thereafter, the physisorbed pyridine was removed by evaporating ($10 \times 10^{-5} \text{ bar}$) the system for 30 min. Next, the pyridine was desorbed in two phases: first, the sample was heated from room temperature to 150°C with a heating ramp of $2.5^\circ\text{C}/\text{min}$ and kept at 150°C for 30 min. After those 30 min a FTIR spectrum was taken. Secondly, the system was heated from 150°C to 550°C with a heating ramp of $10^\circ\text{C}/\text{minute}$ to desorb all pyridine. Every 50°C a FTIR spectrum was taken. The acid site were quantified by band integration derived from Beer's law⁵¹ using literature values for the extinction coefficients.⁵⁷

3.2.6 NH₃-TPD

NH₃-TPD measurements were performed on Micrometer Autochem II equipped with a TCD detector. In the glovebox a sample of 80 mg to 100 mg was prepared. The sample was dried under a He flow by heating it with a heating ramp of 10 °C/min to 200 °C. After 10 minutes the sample was cooled down to 100 °C. At this temperature, ammonia pulses of 25 cm³/min were given until the sample was saturated. The sample was outgassed for 1h at 100 °C to ensure the removal of physisorbed ammonia. Then the ammonia was desorbed by heating the sample to 600 °C with a heating rate of 10 °C/min.

3.2.7 EIS

EIS was measured using a Princeton Applied Research Parstat 2273 in a custom-made measurement cell in a Büchi B585 glass oven. Both the preparation and the measurements were performed in the argon glovebox. Pellets were made by first placing sodium foil (thickness ranging between 0.1 mm and 0.3 mm, 12 mm diameter) on two stainless steel dyes (diameter 13 mm). Between 150 mg and 350 mg sample was placed between the dyes, such that the sample was in contact with the sodium foil. This was pressed at 2.0 metric tonnes of pressure, which is equal to 150.7×10^3 ton/m². The thickness of the pressed pellet was measured and the sample thickness was determined by subtracting the thickness of the dyes and sodium foil (12.88 mm). In a typical EIS measurement, a 20 mV rms modulated AC potential with frequencies ranging from 1 MHz and 1 Hz was applied to the sample. The samples were heated from room temperature to 130 °C with a heating ramp of 5 °C/min. During heating, EIS was measured every 10 °C. Enough time was provided to equilibrate at the temperature before measurement. After heating, the sample cooled down without active cooling. An EIS measurement was performed at 120 °C and from that temperature EIS was measured every 20 °C.

The EIS data was plotted in Nyquist plots. In most cases a semi-circle was observed in the Nyquist plot. The data was fitted using an equivalent circuit consisting of a resistance and a constant phase element. It was assumed that the non-zero intersection of the fitted semicircle with the x-axis represents the the resistance R . The conductivity was calculated using the relation $\sigma = \frac{A}{dR}$, where σ is, the conductivity A is the area, d the thickness of the sample in the pellet. The conductivity was plotted versus the reverse temperature on a logarithmic scale. The data was fitted and the slope of the fit was used to determine the activation energy via the relation $\sigma = Ae^{-E_{Act}/k_B T}$, where σ is the conductivity, E_{Act} the activation energy for ion hopping, k_B the Boltzmann constant and T the temperature.

4 Results and Discussion

In this chapter the results of the synthesis of NaNO_2 based nanocomposites and their conductivity will be given. NaNO_3 nanocomposites were made as well. Since similar results were found for NaNO_3 nanocomposites, the results will not be discussed here, but can be found in the Supporting Information. The chapter will be divided in two parts, each covering a different project. The first project considers melt infiltration of NaNO_2 into six different metal oxides scaffolds. This part will discuss how melt infiltration can be checked and will investigate the influence of different scaffolds on the conductivity. The second part will discuss a model study on the effect of surface groups, in particular the strength of acid sites, on the conductivity. Nanocomposites of NaNO_2 and SiO_2 with different metals atoms anchored to the surface will be studied. The metal grafted on the surface influences the strength of the Lewis sites on the surface of the scaffold, while all other scaffold properties stay the same. This makes these scaffolds useful for a model study.

4.1 Part I: Nanocomposites of different compositions

This first part will provide information about nanocomposites of NaNO_2 confined in the pores of SBA-15 (SiO_2), Al_2O_3 , TiO_2 , Nb_2O_5 , $\text{Nb}_3(\text{PO}_4)_5$ and ZnO_2 . First, the properties of the scaffolds will be stated. Then, several characterization methods will be used to study melt infiltration in the pores SBA-15 and Al_2O_3 extensively. Next, melt infiltration into the other scaffolds (TiO_2 , Nb_2O_5 , $\text{Nb}_3(\text{PO}_4)_5$ and ZrO_2) will be discussed briefly. Thereafter, the conductivity of these nanocomposites will be investigated and factors that might influence the conductivity will be discussed. Finally, the most important conclusions for this part will be summarized and the need for the model study in Part II of the Results and Discussion chapter will be explained.

4.1.1 Scaffolds

SBA-15, $\gamma\text{-Al}_2\text{O}_3$, TiO_2 , Nb_2O_5 , $\text{Nb}_3(\text{PO}_4)_5$ and ZnO_2 were used for nanoconfinement. The six different scaffold have different porosities and surface areas. Physisorption was measured to determine these properties. Figure 4.1 shows the pore size distribution during N_2 adsorption. Further, the pore volume was calculated from the physisorption data with a BJH analysis and the surface area was determined using a BET calculation. These results are summarized in table 4.1. SBA-15 has pores between 7 nm and 10 nm and a high pore volume and BET surface area. Al_2O_3 has pores between 5 nm and 25 nm with an average pore volume and BET surface area. TiO_2 has pore volume and BET surface area as well, but it has a broad pore size distribution, hence no defined pore size. Nb_2O_5 , $\text{Nb}_3(\text{PO}_4)_5$ and ZrO_2 all have low porosity and respectively an average, high and low BET surface area. The pore sizes for $\text{Nb}_3(\text{PO}_4)_5$ and ZrO_2 are between 2 nm and 8 nm for $\text{Nb}_3(\text{PO}_4)_5$ and between 5 nm and 15 nm for $\text{Nb}_3(\text{PO}_4)_5$. Nb_2O_5 has no clear pore size distribution, which is logical given the very low porosity of $0.12 \text{ cm}^3/\text{g}$.

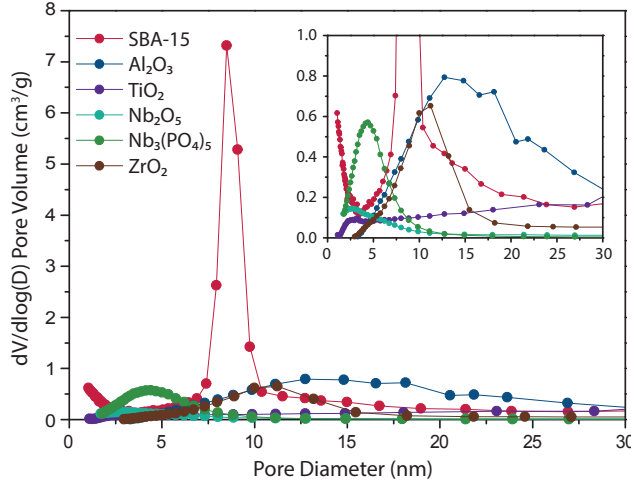


Figure 4.1: Pore size distribution of the metal oxide scaffolds

Scaffold	pore volume (cm ³ /g)	BET surface area (m ² /g)
SBA-15	1.14	787
Al ₂ O ₃	0.45	172
TiO ₂	0.40	105
Nb ₂ O ₅	0.12	143
Nb ₃ (PO ₄) ₅	0.26	255
ZrO ₂	0.26	77

Table 4.1: Pore volume and BET surface area of the metal oxide scaffolds

4.1.2 Nanocomposites

NaNO₂ was melt infiltrated in the pores of the six scaffolds mentioned in the previous section. The following pore fillings were used: 170 % for SBA-15, 130 % for Al₂O₃, 130 % for TiO₂, 200 % for Nb₂O₅, 200 % for Nb₃(PO₄)₅ and 160 % for ZnO₂. Pore fillings of 130 % or higher were used to make sure that not only the pores of the scaffold is filled with salt, but also the outside of the scaffold particles can be covered with the salt. Nanocomposites with lower pore fillings (10 %, 50 %, 70 %) were made as well for NaNO₂ in SBA-15 and in Al₂O₃. These low pore filling nanocomposites were only used to check the success of melt infiltration. Their conductivities were not measured. Using the results of XRD, DRIFTS, N₂-physisorption and DSC for the NaNO₂@SBA-15 and NaNO₂@Al₂O₃ nanocomposites, melt infiltration will be verified in a detailed manner. Thereafter, the results of the other four scaffolds will be discussed briefly.

In order to check melt infiltration, its interesting to know whether the NaNO₂ in the nanocomposites has the same crystalline phases as the pure salt. Therefore, XRD was measured for the two bare scaffolds (SBA-15 and Al₂O₃), for the pure NaNO₂ and for nanocomposites with pore filling of 10 %, 70 %, 130 % (Al₂O₃) and 170 % (SBA-15). Figure 4.2a shows the XRD spectra for these samples. The figure shows that pure NaNO₂ has peaks around 35°, 37°, 52° and 53°. At the highest concentrations (170 % @SBA-15 and 130 % @Al₂O₃) the graphs of both nanocomposites show these peaks as well. This implies that after nanoconfinement crystalline NaNO₂ is present, showing that the materials have not reacted or decomposed during the synthesis. In case of successful melt infiltration, the crystallinity is expected to decrease or even disappear for lower pore fillings due to two effects: first, the amount of salt present decreases and secondly, confined materials lack long range crystallinity due to their nanoscale size and nanoconfinement effects. For the Al₂O₃ nanocomposites this trend is visible, but for the SBA-15 nanocomposites even at a pore filling of 10 % some crystallinity is still visible. Therefore, this XRD spectrum indicates that melt infiltration in the pores of Al₂O₃ was more successful than in the pores of SBA-15.

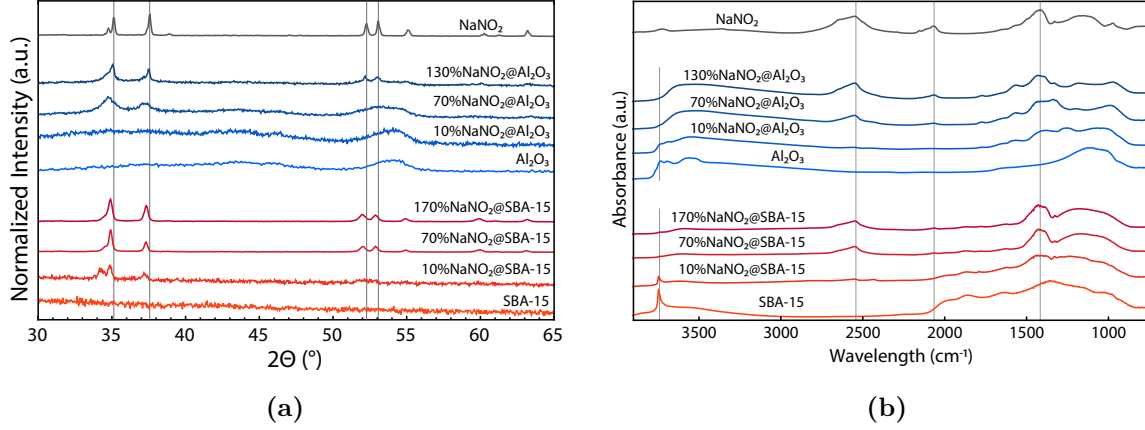


Figure 4.2: (a) XRD of NaNO_2 @SBA-15 and NaNO_2 @ Al_2O_3 nanocomposites with different pore fillings (b) DRIFTS of NaNO_2 @SBA-15 and NaNO_2 @ Al_2O_3 nanocomposites with different pore fillings

Besides the crystallinity of the nanocomposites, molecular vibration of the nanocomposites are interesting as well. DRIFTS measures molecular vibrations, which can be used to determine whether the salt is still present (since the anion NO_2^- has characteristic vibrations) and whether the surface of the scaffold is covered (since the scaffolds have vibrations of OH-surface groups around 3700 cm^{-1}). DRIFTS were taken for the two bare scaffolds (SBA-15 and Al_2O_3), the pure NaNO_2 , and the nanocomposites pore filling of 10 %, 70 %, 130 % (Al_2O_3) and 170 % (SBA-15). Figure 4.2b shows the DRIFT spectra. The nanocomposites of NaNO_2 @SBA-15 and NaNO_2 @ Al_2O_3 have characteristic NaNO_2 vibrations around 2600 cm^{-1} , 2100 cm^{-1} and 1400 cm^{-1} . At higher pore fillings, the surface vibrations of the scaffolds around 3700 cm^{-1} are quenched, at lower pore fillings they reappear. This is a logical trend, as at lower pore filling there is not enough NaNO_2 present to interact with all the surface hydroxyl groups, making it impossible to quench all surface vibrations.

Another approach to check the effectiveness of nanoconfinement is probing the porosity of the nanocomposites by nitrogen physisorption. For this reason physisorption was measured for the bare scaffolds (SBA-15 and Al_2O_3) and the nanocomposites with pore fillings of 50 %, 70 %, 130 % (Al_2O_3) and 170 % (SBA-15). The pore size distribution curves and the total pore volumes at different percentages were used to study the success of melt infiltration. Successful melt infiltration would lead to a decrease in the pore volume of the scaffold material with an increasing amount of NaNO_2 , because the nitrates occupy the pores of the scaffold. Figures 4.3a, 4.3b and 4.3c show the changes in pore size distribution and the trend in remaining porosity for NaNO_2 based nanocomposites. Figure 4.3a shows the pore size distribution curves during N_2 adsorption for the NaNO_2 @SBA-15 nanocomposites. The curves are normalized per gram SBA-15. Only the samples of 0 % pore filling (pure SBA-15) gave adsorption data. This is surprising, since the samples with 50 % and 70 % pore filling should have some remaining porosity. This strongly suggest that the pores are blocked. Figure 4.3b shows the pore size distribution curves for NaNO_2 @ Al_2O_3 . The curves are normalized per gram Al_2O_3 . The nanocomposites with 50 % and 70 % pore filling gave adsorption data, the nanocomposite with 130 % not. This is logical, since the nanocomposites with 50 % and 70 % pore filling should have (remaining) porosity, but nanocomposites with 130 % pore filling not. Furthermore, the figure shows that the decrease in pore volume is larger for the nanocomposite with 70 % pore filling than for the

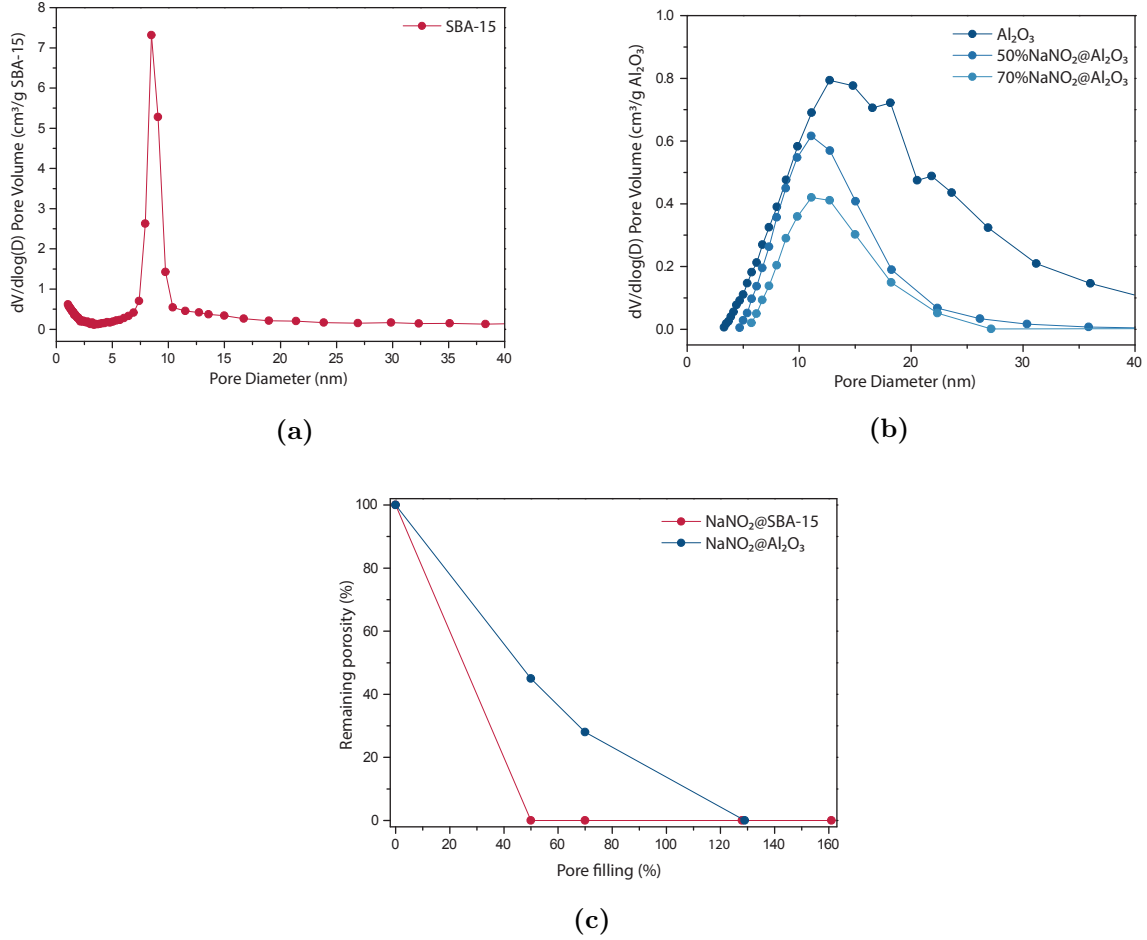


Figure 4.3: (a) Pore size distributions of SBA-15 and NaNO₂@SBA-15 nanocomposites (b) Pore size distribution of Al₂O₃ and NaNO₂@Al₂O₃ nanocomposites (c) Trends in remaining porosity of NaNO₂@SBA-15 and NaNO₂@Al₂O₃ nanocomposites

nanocomposite with 50 % pore filling, which is in line with the higher NaNO₂ content in the the 70 % pore filling nanocomposite. In figure 4.3c the trends in remaining porosity for samples of different pore fillings are visualized. The curves show the remaining porosity calculated from physisorption data versus the pore filling based on the amount of scaffold and salt used. The figure shows that for the NaNO₂@Al₂O₃ nanocomposites the decrease in porosity is in line with the increase in pore filling. For SBA-15 the trend is not logical, since the remaining porosity directly drops to 0%. This is in line with the conclusion mentioned before that probably melt infiltration in SBA-15 was not successful.

DSC was additionally used to monitor the infiltration of the salts in the pores of the scaffold. Especially the presence of a melting peak for nanoconfined material next to the melting peak for bulk material gives information on the success of nanoconfinement. DSC was measured for the pure salts and for the nanocomposites with pore filling 130 % (Al₂O₃) and 170 % (SBA-15). Figure 4.4 shows the DSC graphs and table 4.2 shows two parameters being determined from the graph: the onset temperature of the melting and the melting enthalpy calculated to the mass of NaNO₂. The figure shows NaNO₂ has two phase transitions: a transition from a ferroelectric phase to an anti-ferroelectric phase at 163 °C and melting at 271 °C.⁴⁶

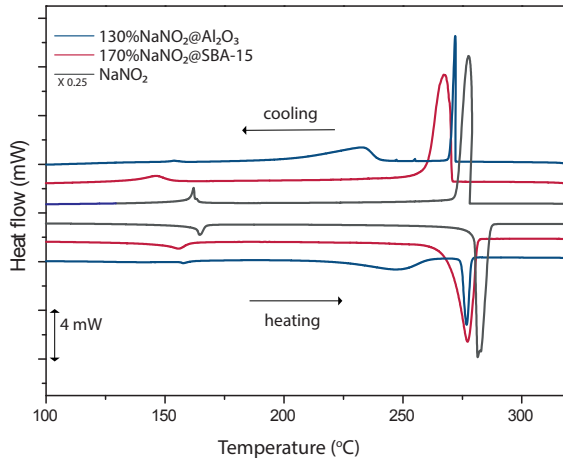


Figure 4.4: DSC of NaNO_2 , the $\text{NaNO}_2@\text{SBA-15}$ nanocomposite and the $\text{NaNO}_2@\text{Al}_2\text{O}_3$ nanocomposite

Nanocomposite $\text{NaNO}_2@$	Onset melting (°C)	Melting Enthalpy (J/g)
- (pure salt)	280	225
SBA-15	270	179
Al_2O_3	275	45

Table 4.2: Onset melting temperature and melting enthalpy for NaNO_2 , the $\text{NaNO}_2@\text{SBA-15}$ nanocomposite and the $\text{NaNO}_2@\text{Al}_2\text{O}_3$ nanocomposite

The SBA-15 nanocomposite has the same two phase transitions as NaNO_2 , although the onset temperature is 10 °C lower and the melting enthalpy is slightly as well. Probably the interactions with the scaffold lower the melting point. For the Al_2O_3 nanocomposite the two peaks from the pure NaNO_2 are still present. The onset melting temperature is a bit lower, but the melting enthalpy is extremely low: it's only 20 % of its original value. This means that only 20 % of all the NaNO_2 in the nanocomposite is present as bulk phase. Next to those two peaks a third, broad peak appeared around 240 °C. This peak can be explained with confinement: nanoconfinement decreases the melting point. Therefore, nanoconfined samples often have two melting peaks: a first peak for confined material and a second for bulk material. Since the exact change in melting point strongly depends on the size of the pores, nanoconfinement peaks are often very broad. This explains both the appearance of a third peak and the reduced melting enthalpy. So the DSC data shows that confinement of NaNO_2 in the pores of Al_2O_3 was successful. The absence of a confinement peak for the SBA-15 nanocomposite suggests that melt infiltration was not successful. However, it is good to keep in mind that nanoconfined materials do not always give an extra peak in DSC. The melting point of nanoconfined materials depends on the particle size and the interface energy between the confined material and the scaffold. If the pores are very small, the phase transition can vanish due to confinement effects and small particle sizes for the confined material. In that case, no peak will be found in the DSC graph for the nanoconfined material.

Taking all the characterization techniques into account, it can be concluded that confinement of the NaNO_2 into Al_2O_3 was successful, but confinement in SBA-15 was not. Besides, it was concluded that investigation of melt infiltration can best be done by a combination of different techniques as one technique might not give sufficient information. Therefore, melt infiltration was checked with DSC, XRD and DRIFTS for TiO_2 , Nb_3O_5 , $\text{Nb}_3(\text{PO}_4)_5$ and ZrO_2 . The DSC, XRD and DRIFTS graphs can be found in the Supporting Information. For TiO_2 and ZrO_2 melt infiltration was successful. For Nb_2O_5 and $\text{Nb}_3(\text{PO}_4)_5$ the results were a bit different. In both the XRD and DRIFTS, the NO_2 peaks disappeared and NO_3 peaks appeared, indicating

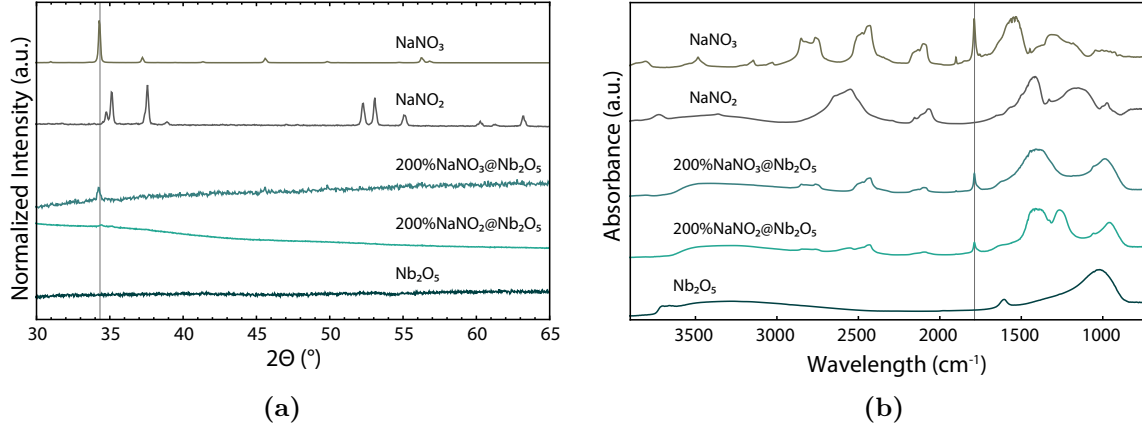


Figure 4.5: (a) XRD of both $\text{NaNO}_2@\text{Nb}_2\text{O}_5$ and $\text{NaNO}_3@\text{Nb}_2\text{O}_5$ nanocomposites (b) DRIFTS of both $\text{NaNO}_2@\text{Nb}_2\text{O}_5$ and $\text{NaNO}_3@\text{Nb}_2\text{O}_5$ nanocomposites

the salt has reacted. In figure 4.5a and 4.5b the XRD and DRIFTS graphs are shown, together with the XRD and DRIFTS results from similar NaNO_3 based nanocomposites to justify the conclusion that the salts have reacted. In DSC the NaNO_2 bulk peaks disappeared. For the Nb_2O_5 nanocomposite two other peaks appeared, for the $\text{Nb}_3(\text{PO}_4)_5$ nanocomposites there were no peaks at all. This indicates that for both niobia nanocomposites the scaffold and salt have reacted. As long as the reaction does not lead to electronic conductivity, this does not have to be a problem.

4.1.3 Conductivity

Having characterized the NaNO_2 based nanocomposites, it is interesting to have a look at their conductivities. The conductivity was derived from the impedance determined for the pure NaNO_2 and the six nanocomposites using EIS. The void fractions of the pellets were calculated using the measured volume (based on the pellet thickness and pellet diameter) and the theoretical volume (based on the densities and weights of the salt and scaffold). The pellet of the pure salt had no void fraction. The pellets of the nanocomposites had void fractions ranging between 8 % and 34 %. Figure 4.6 shows the conductivity for the NaNO_2 samples and table 4.3 shows the activation energies for ion hopping calculated as described in the Experimental Method chapter. The graph shows an increase in conductivity for all the nanocomposites. The increase is the smallest for confinement in SBA-15 (a factor 100) and the largest in Al_2O_3 : over a factor 1000. The conductivity of an electrolyte can be increased in two ways: first of all by changing the amount of ions that move. In the nanocomposites Na^+ ions move via a hopping mechanism, where Na^+ ions hop to vacancies in the structure. Therefore, the amount of ions that move can be changed by adding more ions, but also by introducing more vacancies. Secondly, the conductivity can be changed by changing the hopping mechanism. The activation energy is related to this mechanism. Lower activation energies imply easier hopping mechanisms. The activation energy of the nanocomposites decreased for confinement in the pores of Al_2O_3 , $\text{Nb}_3(\text{PO}_4)_5$ and ZrO_2 , it increased for confinement in the pores of SBA-15 and it stayed the same for confinement in the pores of TiO_2 and Nb_2O_5 . The different activation energies indicate (slightly) different hopping mechanisms for the nanocomposites. However, there is no correlation between the activation energy and the conductivity of the nanocomposites. This is an interesting result, since it means that the increase in conductivity is mainly caused by a change in the amount of ions that move and not by a change in hopping mechanism.

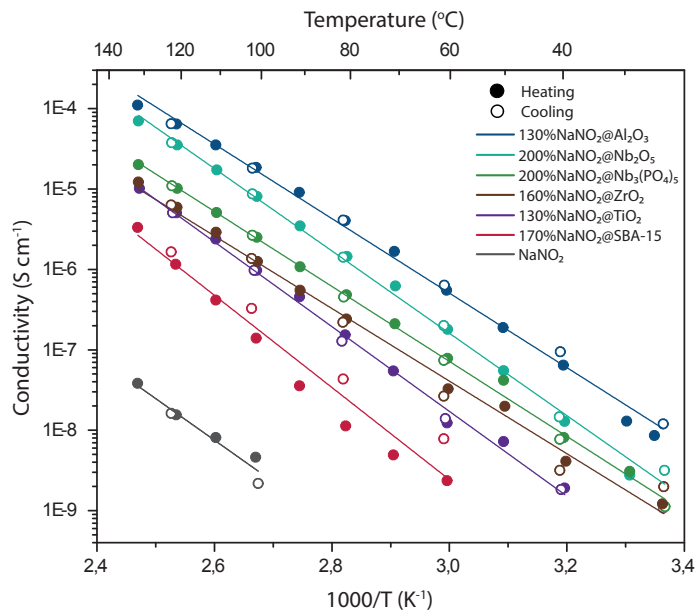


Figure 4.6: Conductivity of NaNO_2 and the NaNO_2 @metaloxides nanocomposites

Nanocomposite NaNO_2 @	Activation energy (eV)
Al_2O_3	0.92
Nb_2O_5	1.02
$\text{Nb}_3(\text{PO}_4)_5$	0.93
ZrO_2	0.90
TiO_2	1.05
SBA-15	1.14
- (pure salt)	1.03

Table 4.3: Activation energies for ion hopping in NaNO_2 and in the NaNO_2 @metaloxides nanocomposites

In the beginning of this chapter it was stated that similar results were found for confinement of NaNO_3 . As a proof, figure 4.7 and table 4.4 show the conductivity and activation energies of the NaNO_3 based nanocomposites. Here, it is good to know that DSC, XRD and DRIFTS (see Supporting Information) showed that melt infiltration was successful for all scaffolds, except for SBA-15. Regarding the conductivities the SBA-15, ZrO_2 and TiO_2 nanocomposites are the worst conducting and the Nb_2O_5 , $\text{Nb}_3(\text{PO}_4)_5$ and Al_2O_3 are the best conducting, just like for the NaNO_2 based nanocomposites. Again, confinement in Al_2O_3 leads to an increase in conductivity over 1000 times. The activation energies are higher for all nanocomposites than for the pure salt, implying a worse hopping mechanism after confinement. There is no correlation between the conductivity and the activation energy, which shows again that the increase in conductivity is mainly caused by a change in amount of moving ions.

For both NaNO_2 and NaNO_3 based nanocomposites there was concluded that the increase in conductivity was due to a change in amount of ions that move. Although the hopping mechanism was not the determining factor for the increase in conductivity, the activation energy for ion hopping changed for almost all the nanocomposites. Therefore, the question rises what caused these differences in conductivity and activation energy of the nanocomposites. Since the nanocomposites consist of different scaffolds, there was looked at differences between the scaffolds. Especially differences between the scaffolds of the best (Al_2O_3) and worst (SBA-15) conducting nanocomposites are interesting. An important difference between SBA-15 and Al_2O_3 , is the the presence of Lewis acid sites. Alumina is known to have Lewis acidity, whilst silica does not. A possible explanation for the differences could be interactions between the sodium salt and acid groups on the surface of the scaffold. To verify this hypothesis, the acid sites on the surface of the six scaffolds were investigated. This was done by pyridine-FTIR and NH_3 -TPD.

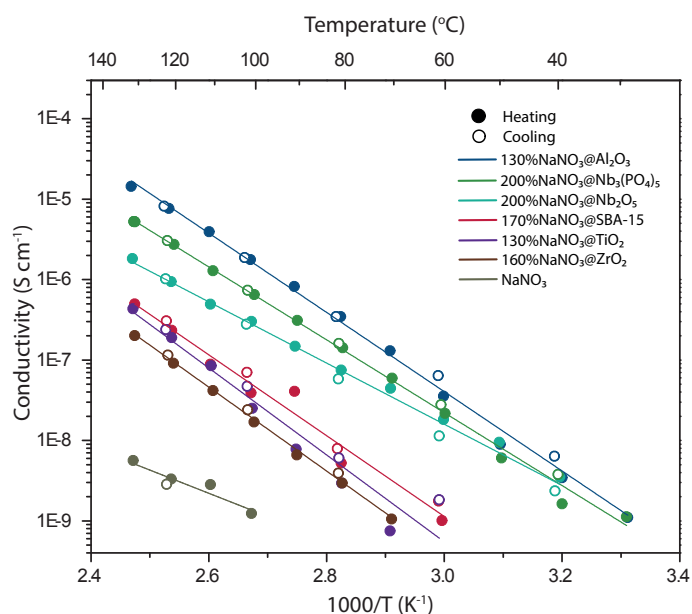
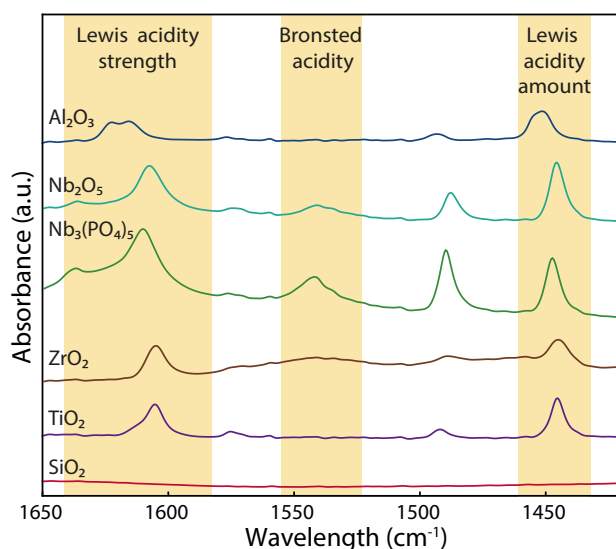


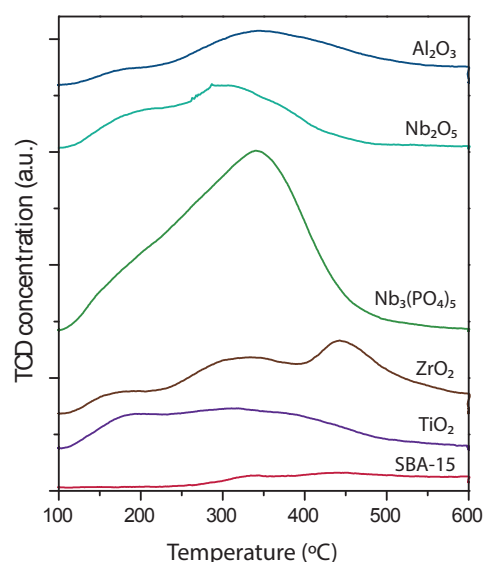
Figure 4.7: Conductivity of NaNO_3 and the NaNO_3 @metaloxides nanocomposites

Nanocomposite NaNO_3 @	Activation energy (eV)
Al_2O_3	0.98
Nb_2O_5	0.75
$\text{Nb}_3(\text{PO}_4)_5$	0.90
ZrO_2	1.03
TiO_2	1.07
SBA-15	1.00
- (pure salt)	0.57

Table 4.4: Activation energies for the ion hopping in NaNO_3 and in the NaNO_3 @metaloxides nanocomposites



(a)



(b)

Figure 4.8: (a) Pyridine-FTIR spectrum of the metal oxide scaffolds at 150 °C (b) NH_3 -TPD spectra of the metal oxide scaffolds

Scaffold	Pyridine FTIR		NH ₃ TPD	
	Ammount (mmol/g)	T _{desorption} (°C)	Ammount (mmol/g)	T _{desorption} (°C)
Al ₂ O ₃	0.049	> 550	0.62	~ 350
Nb ₂ O ₅	0.16	> 500	0.73	~ 360
Nb ₃ (PO ₄) ₅	0.22	> 500	1.82	~ 340
ZrO ₂	0.034	~ 450	0.68	~ 440
TiO ₂	0.14	~ 450	0.71	~ 300
SiO ₂	0	~ 100	0.09	~ 330

Table 4.5: Summary of the results from Pyridine FTIR and NH₃ TPD, giving the amount of acid sites and desorption temperatures of pyrdine and NH₃

There are two facets of acid groups that can influence the conductivity: the amount of the acid sites and the strength of the acid sites. Figure 4.8a shows the FTIR spectrum measured during desorption of pyrdine at 150 °C. The peak at 1450 cm⁻¹ was integrated to determine the amount of Lewis acid sites. The amount of the Brønsted acid sites was determined by integration of the peak around 1545 cm⁻¹.⁴⁹⁻⁵¹ The sum of both Lewis and Brøsted acids sites is given in table 4.5. Figure 4.8b shows the NH₃-TPD graphs. The amounts of acid sites were derived by integration of the peaks in this figure and are given in table 4.5. The values for the amount of acid sites determined with pyrdine-FTIR and NH₃-TPD differ from each other. As the former is known to underestimate and the latter to overestimate the acid sites, this is logical. Both methods show the same trends in the amount of acid sites. The scaffolds in the table are ordered from top to bottom on decreasing conductivity of their NaNO₂ based nanocomposite analogues. The table shows there is no correlation between the amount of acid sites and the conductivity.

Then, it is interesting to look if there is a correlation between the strength of the acid sites and the conductivity. The peak positions in pyridine-FTIR and the desorption temperatures of pyridine and NH₃ give information on the strength of the acid sites. The peak around 1620 cm⁻¹ in figure 4.8a indicates the strength of the Lewis acid site. The stronger the acid site, the more the peak shifts towards higher wavelengths. The strength of the Brønsted acid sites was determined by the peak position of the peak around 1545 cm⁻¹. Again, stronger acid sites lead to shifts towards higher wavelengths. Figure 4.8a shows that Nb₂O₅, Nb₃(PO₄)₅ and maybe ZrO₂ have Brønsted acidity. Except for SBA-15, all scaffolds have Lewis acidity and Al₂O₃ has the strongest acidity. The graphs of the scaffolds are ordered from top to bottom on decreasing conductivity of their NaNO₂ based nanocomposite analogues. There is no correlation between the presence and/or strength of the Brønsted acid sites and the conductivity. Interestingly, going from top to bottom, the strength of the Lewis acid sites decreases. Therefore, the hypothesis is that Lewis acid sites are crucial to high ion conductivity in these nanocomposites. A possible explanation is that the Lewis acid sites enhance the infiltration of the molten sodium salt in the pores of the scaffold and that better infiltration lead to a higher conductivity.

If indeed the acid strength is of importance, then similar correlations should be found between the conductivity and the desorption temperature of pyridine or NH₃. The desorption temperature of NH₃ can be seen in figure 4.8b and the desorption temperatures for pyridine and NH₃ are given in table 4.5. As NH₃ and pyridine are different probe molecules, the absolute values for desorption temperatures cannot be compared. However, the trends should be the same. Indeed, whilst going down in the table, the desorption temperature decreases, so the acid strength decreases. Interestingly, this trend is similar to the trend in conductivity when nanocomposites are made with NaNO₂ and these scaffolds. So this is in line with the hypothesis that the acid site strength influences the conductivity.

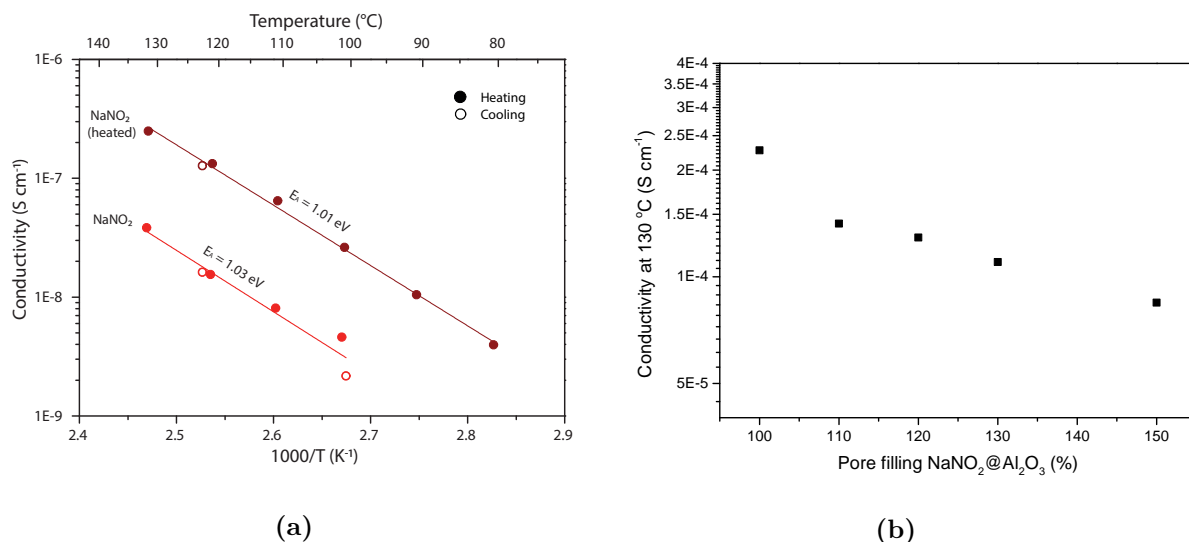


Figure 4.9: (a) Conductivity of NaNO₂ before and after heat treatment (b) trends in conductivity of NaNO₂@Al₂O₃ nanocomposites with different pore fillings

All-in-all, pyridine-FTIR and NH₃-TPD seem to reveal a correlation between the Lewis acid site strength and the conductivity. However, note that there are many factors changing for each scaffold, e.g. the porosity and surface area, which might influence the conductivity as well. Besides, there are several factors other than those related to scaffold properties that might influence the conductivity. Firstly, the void fraction of a pellet influences the conductivity. The pellets used for EIS measurement had a broad range of void fractions, so this already might have influenced the conductivity.

Secondly, the exact structure of the salt including all defects and vacancies can influence the conductivity. Figure 4.9a shows the conductivity of NaNO₂ without heat treatment (shown before) and after heating to the melt infiltration temperature (300 °C). The figure shows that only heating the salt already increases the conductivity. Heating can provide the energy to go to a thermodynamically more stable state with for example less defects. Apparently the structure after heating has a better conductivity.

Thirdly, the conductivity is dependent on the pore filling used. Figure 4.9b shows the trends in conductivity at 130 °C of NaNO₂@Al₂O₃ nanocomposites with different pore fillings ranging between 100 % and 150 %. There was expected to find an optimum in conductivity around 130 % pore filling. The idea of this optimum is that on one hand higher pore fillings have too much bulk material which decreases the conductivity. On the other hand, lower pore fillings have less salt present and therefore cannot at the same time fill the pores and cover the outside of the scaffold particles which decreases the conductivity as well. Surprisingly, this optimum was not found for the nanocomposites measured. Here, lower pore fillings led to higher conductivities. A possible explanation for this results is that the optimum lies around 100 % pore filling. Then, the optimum lies outside the range of pore fillings that was measured. Although a different trend than expected was found, figure 4.9b clearly shows that the pore filling influences the conductivity.

So to conclude, there might be a correlation between the Lewis acid strength of the scaffold and the conductivity, but there are also many other factors that can influence the conductivity, such as the porosity of the scaffold, the surface area of the scaffold and the pore filling used. It is therefore hard to make a fair comparison and a systematic study is need to understand the influence of Lewis acidity on the conductivity.

4.1.4 Summary

In this part, nanocomposites of NaNO_2 into the pores of six different scaffolds (SBA-15, Al_2O_3 , TiO_2 , Nb_2O_5 , $\text{Nb}_3(\text{PO}_4)_5$ and ZrO_2) were made. First, an extensive study was done on the NaNO_2 @SBA-15 and NaNO_2 @ Al_2O_3 nanocomposites to investigate melt infiltration using XRD, DRIFTS, physisorption and DSC. This study showed that melt infiltration of NaNO_2 in the pores of Al_2O_3 was successful, but in the pores of SBA-15 not. Then, melt infiltration of NaNO_2 in the pores of TiO_2 , ZrO_2 , Nb_2O_5 and $\text{Nb}_3(\text{PO}_4)_5$ was discussed briefly using results from XRD, DRIFTS and DSC. For the first two melt infiltration was successful, the last two seemed to have reacted with the scaffold. Next, the conductivity of the nanocomposites was discussed. The conductivity increased upon confinement in all scaffolds, but for confinement in the pores of Al_2O_3 the increase is significantly larger with more than a factor 1000. This gave rise to the question what causes the differences in conductivity. The presence of acid site on the surface of the scaffold was proposed as a factor influencing the conductivity. Pyridine-FTIR and NH_3 -TPD indicated a relation between the strength of the (Lewis) acids sites and the conductivity. However, there are so many factors changing for the scaffolds, that it is difficult to exclude other factors. Hence, a systematic study on the influence of the strength of the acid site is need to draw a reliable conclusion.

4.2 Part II: A systematic study

This part will cover the results of a model system to determine the influence of surface groups, in particular surface acidity, on the conductivity. The scaffolds used in the model system consist of metallocene complexes grafted onto mesoporous silica (Davicat 1404). Figure 4.10 shows the chemical structure of the metal atoms anchored to the silica surface. Seven different metal atoms were grafted to the surface: Hf, Zr, Ti, Mo, Nb, Ta and Ba. Since the metals have different electronegativities, the ionic-character of the M-O bond differs for each scaffold. The ionic-character is related to the acidic strength of the surface groups.^{58,59} Hence, these scaffolds can be used as a model to study the influence of acid sites on the conductivity. NaNO_2 was confined in the seven surface modified scaffolds and the unmodified SiO_2 . First of all, the properties of these eight scaffolds will be investigated. Then, the nanocomposites and their conductivity will be discussed. In the end, the results for this part will be summarized.

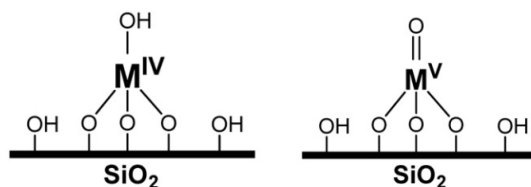


Figure 4.10: Chemical structure of the model system with metallocene complexes grafted to the silica surface. Reprinted from Thornburg et al.⁵⁸

4.2.1 Scaffolds

SiO_2 , SiO_2 -Hf, SiO_2 -Zr, SiO_2 -Ti, SiO_2 -Mo, SiO_2 -Nb, SiO_2 -Ta and SiO_2 -Ba were used as scaffolds for nanocomposites. During the synthesis of these scaffolds it was aimed to put 0.5 metal atoms/ nm^2 on the surface. Inductively coupled plasma (ICP) showed that this was achieved for Hf, Zr, Ti, Nb and Ta. For Mo the amount of atoms/ nm^2 was a little less, 0.4 atoms/ nm^2 and for Ba there was no ICP data.⁵⁶

Physisorption data was measured for SiO_2 , SiO_2 -Ti and SiO_2 -Nb. Figure 4.11 shows the pore size distribution of the scaffolds and table 4.6 summarizes the pore volume and surface area calculated with respectively BJH and BET analysis. The figure shows that all three scaffolds have a similar pore size distribution between 3 nm and 20 nm. The porosity and surface area seem to slightly decrease upon grafting metal atoms to the SiO_2 surface. However, it was concluded that the porosity and surface area are similar enough to use these scaffolds as model system.

4.2.2 Nanocomposites

Nanocomposites were made with 130 % pore filling of NaNO_2 in the pores of SiO_2 , SiO_2 -Hf, SiO_2 -Zr, SiO_2 -Ti, SiO_2 -Mo, SiO_2 -Nb, SiO_2 -Ta and SiO_2 -Ba. Melt infiltration of the nanocomposites was checked with DSC, XRD and DRIFTS. The data can be found in the Supporting Information. It was concluded that melt infiltration was successful for all nanocomposites, with the exception of NaNO_2 @ SiO_2 -Nb.

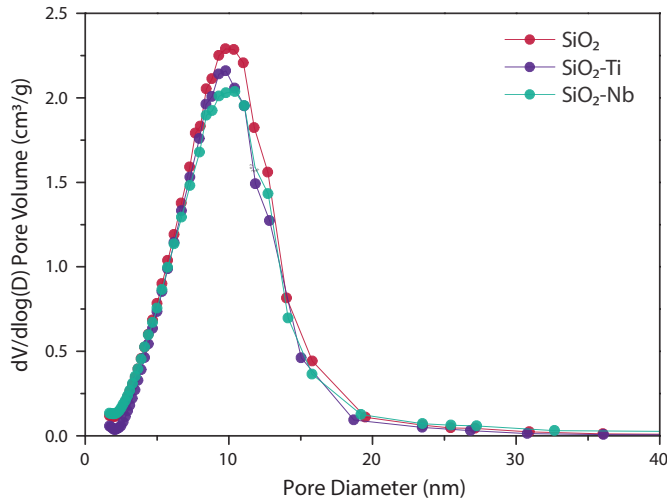


Figure 4.11: Pore size distribution of some of the SiO_2 scaffolds with metal atoms grafted on the surface

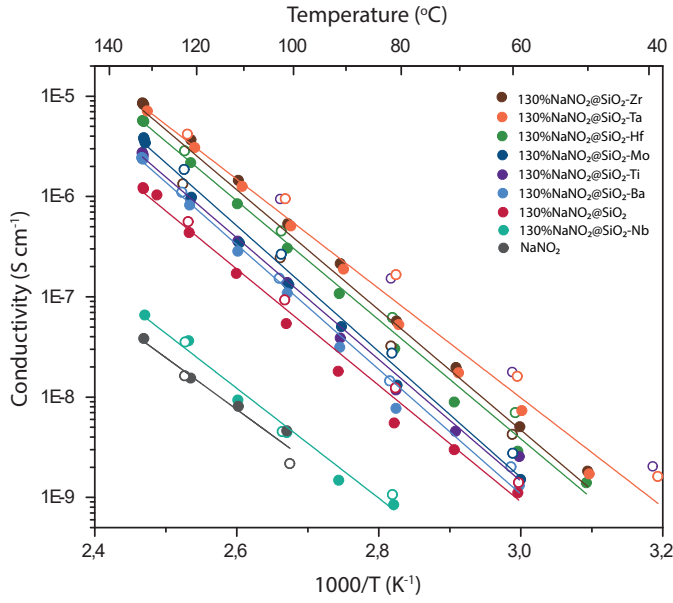
Scaffold	porosity (cm^3/g)	BET surface area (m^2/g)
SiO_2	0.92	526
$\text{SiO}_2\text{-Ti}$	0.81	437
$\text{SiO}_2\text{-Nb}$	0.0.87	492

Table 4.6: Porosity and surface area of some of the SiO_2 scaffolds with metal atoms grafted on the surface

4.2.3 Conductivity

The conductivity was measured for all nanocomposites and is given in figure 4.12. The activation energies for ion hopping are given in table 4.7. All nanocomposites have a conductivity within one order of magnitude, except for the $\text{SiO}_2\text{-Nb}$ nanocomposites. Most likely this nanocomposite has a worse conductivity, since melt infiltration was not successful. The activation energy increases upon confinement and ranges from 1.08 eV for $\text{NaNO}_2@\text{SiO}_2\text{-Ta}$ to 1.24 eV for $\text{NaNO}_2@\text{SiO}_2\text{-Mo}$. The activations energies differ only slightly and there is no logical correlation between the activation energy and the conductivity. This means that the increase in conductivity is mainly caused by a change in the amount of moving ions (and not by a change in hopping mechanism). Based on the conductivity of the nanocomposites ($\text{NaNO}_2@\text{SiO}_2\text{-Nb}$ excluded), a few conclusions can be drawn. First of all, it is clear that nanoconfinement increases the conductivity in comparison to the pure salt. Secondly, out of these seven nanocomposites, the SiO_2 is the worst conducting. So the addition of metal atoms to the silica surface leads to an increase in conductivity. Unfortunately, figure 4.12 is overfull and therefore it is difficult to make a proper distinction between curves of different nanocomposites and to draw conclusions about the relation between the type of metal atom on the surface and the conductivity.

For this reason, figure 4.13 shows the conductivities of the nanocomposites at 130 °C versus the ionic character of the M-O bond. For each data point the metal on the surface of the scaffold in the nanocomposite is given. Here, a correlation between the ionic character and the conductivity was expected. A linear trend could have been explained by the fact that a stronger acid leads to better melt infiltration and therefore better conductivity. Also a volcano-plot-like behaviour could have been explained. This could be caused by a combined effect of on one hand better melt infiltration of the salt for stronger acid sites increasing the conductivity, but on the other hand too strong binding of the salt to the surface for stronger acid sites decreasing the conductivity. However, neither of them is the case. There is no correlation between the data points. Therefore, the question rises what caused the difference in conductivity, because there clearly are differences in conductivity.



Nanocomposite NaNO ₂ @	Activation energy (eV)
SiO ₂ -Zr	1.19
SiO ₂ -Ta	1.08
SiO ₂ -Hf	1.18
SiO ₂ -Mo	1.24
SiO ₂ -Ti	1.20
SiO ₂ -Ba	1.23
SiO ₂	1.15
SiO ₂ -Nb	1.09
NaNO ₂	1.03

Figure 4.12: Conductivity of nanocomposites of NaNO₂ and SiO₂ scaffolds with metal atoms grafted on the surface

Table 4.7: Activation energies for ion hopping in the nanocomposites of NaNO₂ and SiO₂ scaffolds with metal atoms grafted on the surface

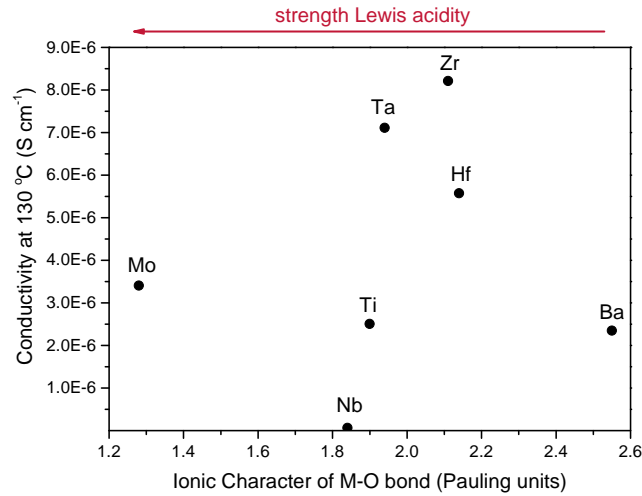


Figure 4.13: Conductivity of the nanocomposites of NaNO₂ and SiO₂ scaffolds with metal atoms grafted on the surface at 130 °C versus the ionic character of the M-O bond

The model study was set up to exclude factors such as porosity, surface area, and number of surface groups per square nanometer. Analysis of the scaffold shown in the section Scaffolds illustrated the scaffolds are comparable on this level. However, the scaffolds were characterized directly after their synthesis. Before the nanocomposites were made, they were stored for several months under air. Some of the scaffolds, e.g. the SiO₂-Mo, are known to react with water in the air breaking the bonds between the silica and the metal. Given the long time the scaffolds were exposed to air, reaction of the scaffolds with water cannot be excluded. Then, it is no

longer certain that the number of surface group per square nanometers was equal for all the scaffolds. Hence, the model used might not have been a good model. To conclude, it is unclear if the results about the nanocomposites discussed in Part II are reliable. Therefore, the data cannot be used to draw a conclusion about the relation between acid sites on the surface of the scaffold and the conductivity of NaNO_2 based nanocomposites. To be able to do so, the experiments would have to be repeated. This time, the scaffold must be stored under inert atmosphere directly after synthesis.

4.2.4 Summary

This part used a model system of metal atoms grafted to silica in order to investigate the influence of acid groups on the surface of the scaffold on the conductivity of a NaNO_2 based nanocomposite. At first, the model system seemed to be suitable and the nanocomposites were successfully synthesized with melt infiltration (a single exception excluded). The conductivity was determined for all nanocomposites and a few conclusion were drawn from these results. The nanocomposites had conductivities within one order of magnitude that were all significantly higher than the conductivity of the pure salt. So confinement is a successful method to increase the conductivity of NaNO_2 . Also, the nanocomposites with metal atoms grafted to the surface had higher conductivities than the nanocomposites with the pure silica. So metal atoms on the surface improve the conductivity. Unfortunately, it turned out impossible to find a correlation between properties of the metal atom and the conductivity. Over and above this, it was found that the scaffolds might have degraded over time, putting the reliability of this model study under debate. Hence, to be able to draw a conclusion about the relation between the acid groups on the surface of the scaffold and the conductivity, the experiments must be repeated, ensuring that the scaffold are stored in an inert atmosphere.

5 Conclusions and Outlook

In this work, the conductivity of NaNO_2 based nanocomposites was determined together with factors influencing the conductivity. Firstly, nanocomposites of NaNO_2 and SBA-15 (SiO_2), Al_2O_3 , TiO_2 , Nb_2O_5 , $\text{Nb}_3(\text{PO}_4)_5$ and ZrO_2 were synthesized via melt infiltration. It was shown that for all nanocomposites, with the exception of NaNO_2 @SBA-15, confinement was successful. EIS measurement showed that all the nanocomposites had an increased conductivity, exceeding a factor 1000 increase for confinement in Al_2O_3 . Results from pyridine-FTIR and NH_3 -TPD suggest a correlation between the strength of the acid site and the conductivity. However, there are other factors like the porosity and surface area that vary for each scaffold as well. Therefore, a model study was performed to investigate the influence of acid sites. In this study, NaNO_2 was confined in porous SiO_2 with different metal (Hf, Zr, Ti, Mo, Nb, Ta, Ba) atoms anchored to the surface of the scaffold. Different metals give rise to a different ionic character of the M-O bond, which can be related to the Lewis acidity. Melt infiltration was successful except for the NaNO_2 @ SiO_2 -Nb nanocomposite. The conductivity of the nanocomposites was higher than for the pure salt, with exception of the NaNO_2 @ SiO_2 -Nb nanocomposite. Conductivity measurements showed that the presence of metal atoms improves the conductivity. However, it turned out to be impossible to relate the change in conductivity to the electronegativity of the metal atoms. There is doubt as to whether the scaffolds were stable. As a result of this, the experiments need to be repeated in order to draw a justified conclusion.

Therefore, repeating the model study whilst ensuring that the scaffolds do not react with air or water is the first part of the outlook. This would provide information about the influence of acid surface groups. If a logical correlation is found, the trend could be applied to engineer a scaffold that would improve the conductivity to a maximum. Furthermore, understanding factors that influence the conductivity could be applied to other combinations of salt and scaffolds as well. If it turns out to be impossible to perform the model study, ball milling may be worth investigating. Ball milling is another synthesis method to make nanocomposites. Ball milling removes porosity and creates interfaces between the salt and scaffolds by crushing them extremely thoroughly. Eliminating the effect of having different porosities leads to nanocomposites that can be compared. Moreover, it could be useful to measure chronoamperometry and cyclic voltammetry of the nanocomposites. These measurements can provide information about respectively the type of charge carriers causing the conductivity (anions, cations or electrons) and the stability of the nanocomposites. Hopefully, these experiments can lead to complete and fundamental understanding of the influence of surface interactions on the ion conductivity of NaNO_2 based nanocomposites and explain the boost in ion conductivity that was found for the nanocomposites in this work.

6 A Laymen's Summary

The energy demand increases annually. At the same time, the emission of CO_2 should be reduced in order to fulfil the Paris agreements of not exceeding a global warming of 2°C . Therefore, it is necessary to shift from fossil fuels to renewable energy sources. An important drawback of renewable energy sources is their intermittent nature, resulting in an unpredictable and varying energy supply. Energy storage, however, can solve this problem. Energy can be stored in multiple ways, but storing energy in batteries appears to be a promising option. Currently, lithium-ion batteries are the most utilized battery. However, lithium batteries are less suited for energy storage on a large scale, since the metal is relatively scarce and consequently more costly. Hence, other metals are being investigated. Sodium seems promising, since it is available in abundance, cheap and chemically similar to lithium. Currently, sodium batteries do exist, but unfortunately they operate only at 300°C . The reason for this is that one part of the battery, a solid called the electrolyte, has poor contact with other parts of the battery at lower temperatures. Therefore, a substantial amount of research is being carried out to find better electrolytes. There are quite a number of requirements to be met for those electrolytes, for example; they need to conduct ions, be stable and they must have a good interface with other parts of a battery. To date, an electrolyte fulfilling all these requirements has not been synthesized.

In this research, a specific type of a low-cost electrolyte was investigated. This electrolyte consists of a mixture of a sodium salt, NaNO_2 , and a matrix. The mixture was heated so that the salt melted into the matrix. Such a molten mixture is called a nanocomposite. In this work, the ion conductivity of NaNO_2 based nanocomposites and factors that influence the conductivity were studied. Therefore, nanocomposites of NaNO_2 molten into different matrices were synthesized. First, a method was set-up to check that the melting process ran successful. Then, the conductivity was measured and it was found that for the nanocomposites the conductivity was between 100 and more than 1000 times better than for the pure NaNO_2 . The best conductivity was found for a nanocomposite of NaNO_2 and Al_2O_3 . Next, the cause of the increase in conductivity was analysed. Analysis of the matrices indicated that acid groups on the surface of the matrix might play an important role. However, there were also many other parameters changing, making it hard to draw conclusions. Therefore, a systematic study was done to understand the influence of acid groups. This study made use of matrices that differed on only one single aspect, which was related to the acidity. Although the study showed that acid groups do play a role, it was impossible to quantify those trends. It turned out that the matrices were old and therefore might have changed. Then, it no longer holds that one single aspect was studied. The study needs to be repeated to draw a conclusion about the effect of acidity on the surface. So, although more research is needed to fully understand the surface interactions in these nanocomposites, this work gave more insight into the use of NaNO_2 based nanocomposites as electrolytes for batteries and showed that nanocomposites are promising to boost the conductivity of NaNO_2 .

Acknowledgement

After working on this thesis over the past year, there are many people I would like to thank. Firstly, I would like to thank dr. Peter Ngene for being my supervisor, for the extensive discussions about results and endless and creative ideas for new experiments. I thank prof. Petra de Jongh for the opportunity to perform my master thesis at the *Inorganic Chemistry and Catalysis* group. I would like to thank Laura de Kort for teaching me the labs skills required and for answering all my (practical) questions. I thank Matt Peerling for the close collaboration on solid-state electrolytes, sharing experiments and daily conversations. I would like to thank all the members of the battery meetings for the interesting discussions. I thank Jan Willem de Rijk for the help in fixing problems at the H₂-lab.

Johan de Boed is gratefully acknowledged for the synthesis of the silica's with metallocene complexes grafted onto the surface. Sylvia Zanoni is acknowledged for measuring physisorption and teaching me how to measure pyrdine-FTIR. Petra Keijzer is acknowledged for the help in the synthesis of SBA-15 and Carlos Hernandez Meija is acknowledged for the supply of Nb₂O₅ and Nb₃(PO₄)₅.

Finally, I would like to thank all the members of the ICC research group for making it a pleasant working place for my master thesis, both on a academic level (with interesting discussions multiple times per week) and for social activities (like 'borrels', lab outings and Christmas dinners). I want to thank all master students for their support, conversations and master meetings with cookies!

Bibliography

- [1] IEA. Global energy and co2 status report 2019. <https://www.iea.org/reports/global-energy-and-co2-status-report-2019>, 2019.
- [2] UN Framework Convention on Climate Change. Adoption of the paris agreement. Technical report, 2015.
- [3] T. M.I. Mahlia, T J Saktisahdan, A Jannifar, M H Hasan, and H. S.C. Matseelar. A review of available methods and development on energy storage; Technology update. *Renewable and Sustainable Energy Reviews*, 33:532–545, 2014.
- [4] Scientific background on the nobel prize in chemistry. *Nobel Prize*, 2019.
- [5] Jang Yeon Hwang, Seung Taek Myung, and Yang Kook Sun. Sodium-ion batteries: Present and future. *Chemical Society Reviews*, 46(12):3529–3614, 2017.
- [6] Chen Xi Zu and Hong Li. Thermodynamic analysis on energy densities of batteries. *Energy and Environmental Science*, 4(8):2614–2624, 2011.
- [7] Verónica Palomares, Paula Serras, Irune Villaluenga, Karina B Hueso, Javier Carretero-González, and Teófilo Rojo. Na-ion batteries, recent advances and present challenges to become low cost energy storage systems. *Energy and Environmental Science*, 5(3):5884–5901, 2012.
- [8] Tiexin Li, Jing Xu, Chengyin Wang, Wenjian Wu, Dawei Su, and Guoxiu Wang. The latest advances in the critical factors (positive electrode, electrolytes, separators) for sodium-sulfur battery. *Journal of Alloys and Compounds*, 792:797–817, 2019.
- [9] Yumei Wang, Shufeng Song, Chaohe Xu, Ning Hu, Janina Molenda, and Li Lu. Development of solid-state electrolytes for sodium-ion battery—A short review. *Nano Materials Science*, 1(2):91–100, 2019.
- [10] Bruce Dunn, Haresh Kamath, and Jean Marie Tarascon. Electrical energy storage for the grid: A battery of choices. *Science*, 334(6058):928–935, 2011.
- [11] Meridian International Research. The sodium-nickel chloride zebra battery. pages 104–112.
- [12] Weidong Zhou, Yutao Li, Sen Xin, and John B Goodenough. Rechargeable Sodium All-Solid-State Battery. *ACS Central Science*, 3(1):52–57, 2017.
- [13] John B Goodenough and Kyu Sung Park. The Li-ion rechargeable battery: A perspective. *Journal of the American Chemical Society*, 135(4):1167–1176, 2013.

- [14] P. E. de Jongh, D. Blanchard, M. Matsuo, T. J. Udovic, and S. Orimo. Complex hydrides as room-temperature solid electrolytes for rechargeable batteries. *Applied Physics A: Materials Science and Processing*, 122(3), 2016.
- [15] Hanna He, Dan Sun, Yougen Tang, Haiyan Wang, and Minhua Shao. Understanding and improving the initial Coulombic efficiency of high-capacity anode materials for practical sodium ion batteries. *Energy Storage Materials*, 23:233–251, 2019.
- [16] Huilin Pan, Yong Sheng Hu, and Liquan Chen. Room-temperature stationary sodium-ion batteries for large-scale electric energy storage. *Energy and Environmental Science*, 6(8):2338–2360, 2013.
- [17] R. H. Radzilowski, Y. F. Yao, and J. T. Kummer. Dielectric loss of beta alumina and of ion-exchanged beta alumina. *Journal of Applied Physics*, 40(12):4716–4725, 1969.
- [18] Alexandre Ponrouch and M Rosa Palacín. Post-Li batteries : promises and challenges Subject Areas :. *Phil. Trans. R. Soc.*, 377, 2019.
- [19] Alexandre Ponrouch, Elena Marchante, Matthieu Courty, Jean-Marie Tarascon, and M Rosa Palac. In search of an optimized electrolyte for Na-ion batteries. *Energy and Environmental Science*, 5:8572–8583, 2012.
- [20] K. B. Md Isa, L. Othman, D. Hambali, and Z. Osman. Electrical and electrochemical studies on sodium ion-based gel polymer electrolytes. *AIP Conference Proceedings*, 1877(1):040001, 2017.
- [21] Deepak Kumar and S A Hashmi. Ionic liquid based sodium ion conducting gel polymer electrolytes. *Solid State Ionics*, 181(8-10):416–423, 2010.
- [22] R C Agrawal and G P Pandey. Solid polymer electrolytes: materials designing and all-solid-state battery applications: an overview. *Journal of Physics D: Applied Physics*, 41(22):223001, oct 2008.
- [23] J.B. Goodenough, H.Y-P. Hong, and J.A. Kafalas. Fast na-ion transport in skeleton structures. *Materials Research Bulletin*, 11(2):203 – 220, 1976.
- [24] H.Y-P. Hong. Crystal structures and crystal chemistry in the system $na_{1+x}zr_2si_xp_{3-x}o_{12}$. *Materials Research Bulletin*, 11(2):173 – 182, 1976.
- [25] Mojtaba Samiee, Balachandran Radhakrishnan, Zane Rice, Zhi Deng, Ying Shirley Meng, Shyue Ping Ong, and Jian Luo. Divalent-doped $Na_3Zr_2Si_2PO_{12}$ natrium superionic conductor: Improving the ionic conductivity via simultaneously optimizing the phase and chemistry of the primary and secondary phases. *Journal of Power Sources*, 347:229–237, 2017.
- [26] Motoaki Matsuo, Shingo Kuromoto, Toyoto Sato, Hiroyuki Oguchi, Hitoshi Takamura, and Shin Ichi Orimo. Sodium ionic conduction in complex hydrides with [BH 4] - and [NH 2] - anions. *Applied Physics Letters*, 100(20):203904, 2012.
- [27] Terrence J Udovic, Motoaki Matsuo, Atsushi Unemoto, Nina Verdal, Vitalie Stavila, Alexander V Skripov, John J Rush, Hitoshi Takamura, and Shin Ichi Orimo. Sodium superionic conduction in $Na_2B_{12}H_{12}$. *Chemical Communications*, 50(28):3750–3752, 2014.

- [28] Terrence J. Udovic, Motoaki Matsuo, Wan Si Tang, Hui Wu, Vitalie Stavila, Alexei V. Soloninin, Roman V. Skoryunov, Olga A. Babanova, Alexander V. Skripov, John J. Rush, Atsushi Unemoto, Hitoshi Takamura, and Shin Ichi Orimo. Exceptional superionic conductivity in disordered sodium decahydro-closo-decaborate. *Advanced Materials*, 26(45):7622–7626, 2014.
- [29] H Oguchi, M Matsuo, S Kuromoto, H Kuwano, and S Orimo. Sodium-ion conduction in complex hydrides NaAlH₄ and Na₃AlH₆. *Journal of Applied Physics*, 111(3):36102, 2012.
- [30] Atsushi Unemoto, Motoaki Matsuo, and Shin Ichi Orimo. Complex hydrides for electrochemical energy storage. *Advanced Functional Materials*, 24(16):2267–2279, 2014.
- [31] Didier Blanchard, Angeloclaudio Nale, Dadi Sveinbjörnsson, Tamara M. Eggenhuisen, Margriet H.W. Verkuijlen, Suwarno, Tejs Vegge, Arno P.M. Kentgens, and Petra E. De Jongh. Nanoconfined LiBH₄ as a fast lithium ion conductor. *Advanced Functional Materials*, 25(2):184–192, 2015.
- [32] Oscar Brandt Corstius. Novel interface-engineered sodium-based nanocomposites as solid-state-electrolytes. *masterthesis, unpublished*, 2019.
- [33] Yong Seok Choi, Young Su Lee, Kyu Hwan Oh, and Young Whan Cho. Interface-enhanced Li ion conduction in a LiBH₄-SiO₂ solid electrolyte. *Physical Chemistry Chemical Physics*, 18(32):22540–22547, 2016.
- [34] Yong Seok Choi, Young Su Lee, Dong Jun Choi, Keun Hwa Chae, Kyu Hwan Oh, and Young Whan Cho. Enhanced Li Ion Conductivity in LiBH₄-Al₂O₃ Mixture via Interface Engineering. *Journal of Physical Chemistry C*, 121(47):26209–26215, 2017.
- [35] Peter Ngene, Sander F.H. Lambregts, Didier Blanchard, Tejs Vegge, Manish Sharma, Hans Hagemann, and Petra E De Jongh. The influence of silica surface groups on the Li-ion conductivity of LiBH₄/SiO₂ nanocomposites. *Physical Chemistry Chemical Physics*, 21(40):22456–22466, 2019.
- [36] Jiaxin Zheng, Guoyu Tan, Peng Shan, Tongchao Liu, Jiangtao Hu, Yancong Feng, Luyi Yang, Mingjian Zhang, Zonghai Chen, Yuan Lin, Jun Lu, Joerg C Neufeind, Yang Ren, Khalil Amine, Lin Wang Wang, Kang Xu, and Feng Pan. Understanding Thermodynamic and Kinetic Contributions in Expanding the Stability Window of Aqueous Electrolytes. *Chem*, 4(12):2872–2882, 2018.
- [37] Jianbo Jiang, Beibei Liu, Guiyu Liu, Dong Qian, Chunming Yang, and Junhua Li. A systematically comparative study on LiNO₃ and Li₂SO₄ aqueous electrolytes for electrochemical double-layer capacitors. *Electrochimica Acta*, 274:121 – 130, 2018.
- [38] Axel Gambou-Bosca and Daniel Bélanger. Electrochemical characterization of MnO₂-based composite in the presence of salt-in-water and water-in-salt electrolytes as electrode for electrochemical capacitors. *Journal of Power Sources*, 326:595 – 603, 2016.
- [39] Petra E. De Jongh and Tamara M. Eggenhuisen. Melt infiltration: An emerging technique for the preparation of novel functional nanostructured materials. *Advanced Materials*, 25(46):6672–6690, 2013.
- [40] Stephen Brunauer, D. L. Kantro, and C. H. Weise. The surface energies of amorphous silica and hydrous amorphous silica. *Canadian Journal of Chemistry*, 34(10):1483–1496, 1956.

- [41] M. L. Guzmán-Castillo, X Bokhimi, A. Rodríguez-Hernández, A Toledo-Antonio, F. Hernández-Beltrán, and J J Fripiat. The surface energy of quasi-amorphous γ alumina calculated from the temperature of the γ to α transition. *Journal of Non-Crystalline Solids*, 329(1-3):53–56, 2003.
- [42] H Bloom, F G Davis, and D W James. Molten salt mixtures. Part 4. - The surface tension and surface heat content of molten salts and their mixtures. *Transactions of the Faraday Society*, 56:1179–1186, 1960.
- [43] Matthias Thommes, Katsumi Kaneko, Alexander V Neimark, James P Olivier, Francisco Rodriguez-Reinoso, Jean Rouquerol, and Kenneth S.W. Sing. Physisorption of gases, with special reference to the evaluation of surface area and pore size distribution (IUPAC Technical Report). *Pure and Applied Chemistry*, 87(9-10):1051–1069, 2015.
- [44] Stephen Brunauer, P H Emmett, and Edward Teller. Adsorption of Gases in Multimolecular Layers. *Journal of the American Chemical Society*, 60(2):309–319, 1938.
- [45] Elliott P Barrett, Leslie G Joyner, Paul P Halenda Vol, $R_nAV_n - R_nAtn Apj$, and $R_n A V_n - R_n Atn Ac$. The determination of pore volume and area distribution in porous substances. computations from nitrogen isotherms. Technical report, 1951.
- [46] Yasusada Yamada, Iwao Shibuya, and Sadao Hoshino. Phase transition in nano2. *Journal of the Physical Society of Japan*, 18(11):1594–1603, 1963.
- [47] E. R. Johnson, A. Frances, and C. Cm. Wu. Phase transition in nano3. *Journal of Applied Physics*, 47(5):1827–1828, 1976.
- [48] Rolf W Berg, David H Kerridge, and Peter H Larsen. $NaNO_2 + NaNO_3$ phase diagram: New data from DSC and raman spectroscopy. *Journal of Chemical and Engineering Data*, 51(1):34–39, 2006.
- [49] E. P. Parry. An infrared study of pyridine adsorbed on acidic solids. Characterization of surface acidity. *Journal of Catalysis*, 2(5):371–379, 1963.
- [50] Claudio Morterra, Anna Chiorino, Giovanna Ghiotti, and Edoardo Garrone. Surface acidity of η -alumina. Part 1. - Pyridine chemisorption at room temperature. *Journal of the Chemical Society, Faraday Transactions 1: Physical Chemistry in Condensed Phases*, 75:271–288, 1979.
- [51] Marjolein Velthoen. *Lewis Acidity in Cracking and Polymerization Catalysis*. PhD thesis, Utrecht University, 2019.
- [52] Tommy Barzetti, Elena Selli, Daniele Moscotti, and Lucio Forni. Pyridine and ammonia as probes for FTIR analysis of solid acid catalysts. *Journal of the Chemical Society - Faraday Transactions*, 92(8):1401–1407, 1996.
- [53] Ben Ern . Lecture notes on Colloidal Analysis Techniques, 2018.
- [54] Hyung Ik Lee, Jin Hoe Kim, Galen D Stucky, Yifeng Shi, Chanhok Pak, and Ji Man Kim. Morphology-selective synthesis of mesoporous SBA-15 particles over micrometer, submicrometer and nanometer scales. *Journal of Materials Chemistry*, 20(39):8483–8487, 2010.
- [55] Thomas Maschmeyer, Fernando Rey, Gopinathan Sankar, and John Meurig Thomas. Heterogeneous catalysts obtained by grafting metallocene complexes onto mesoporous silica. *Nature*, 378(6553):159–162, 1995.

- [56] E.J.J. de Boed, P.E. de Jongh, and B. Donoeva. *in preparation*, 2020.
- [57] C.A. Emeis. Determination of integrated molar extinction coefficients for infrared absorption bands of pyridine adsorbed on solid acid catalysts. *Journal of Catalysis*, 141:347–354, 1993.
- [58] Nicholas E. Thornburg, Anthony B. Thompson, and Justin M. Notestein. Periodic Trends in Highly Dispersed Groups IV and V Supported Metal Oxide Catalysts for Alkene Epoxidation with H₂O₂. *ACS Catalysis*, 5(9):5077–5088, 2015.
- [59] I D Brown and A Skowron. Electronegativity and Lewis Acid Strength. *J. Am. Chem. Soc.*, 112:3401–3403, 1990.

Appendix

6.1 A: Supporting information

6.1.1 NaNO_2

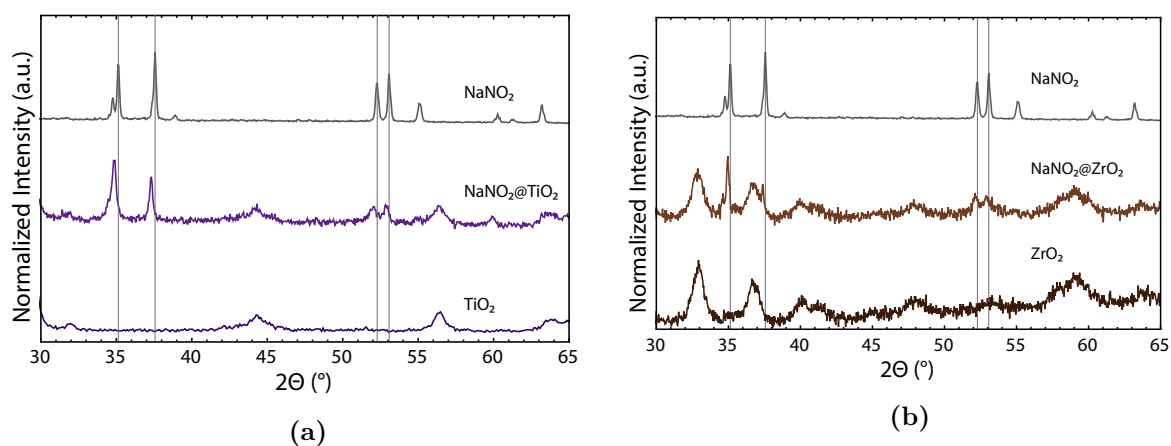


Figure 6.1: (a) XRD of the $\text{NaNO}_2@\text{TiO}_2$ nanocomposite (b) XRD of the $\text{NaNO}_2@\text{ZrO}_2$ nanocomposite

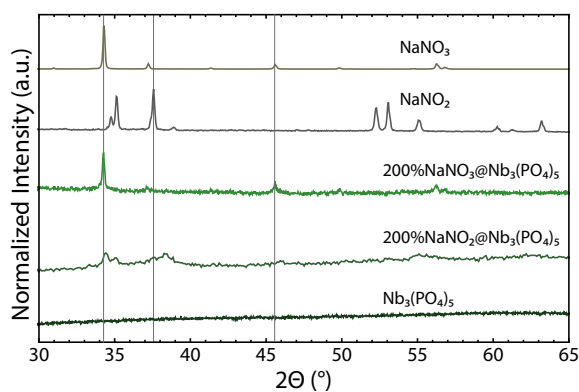


Figure 6.2: XRD of the $\text{NaNO}_2@\text{Nb}_3(\text{PO}_4)_5$ and $\text{NaNO}_3@\text{Nb}_3(\text{PO}_4)_5$ nanocomposites

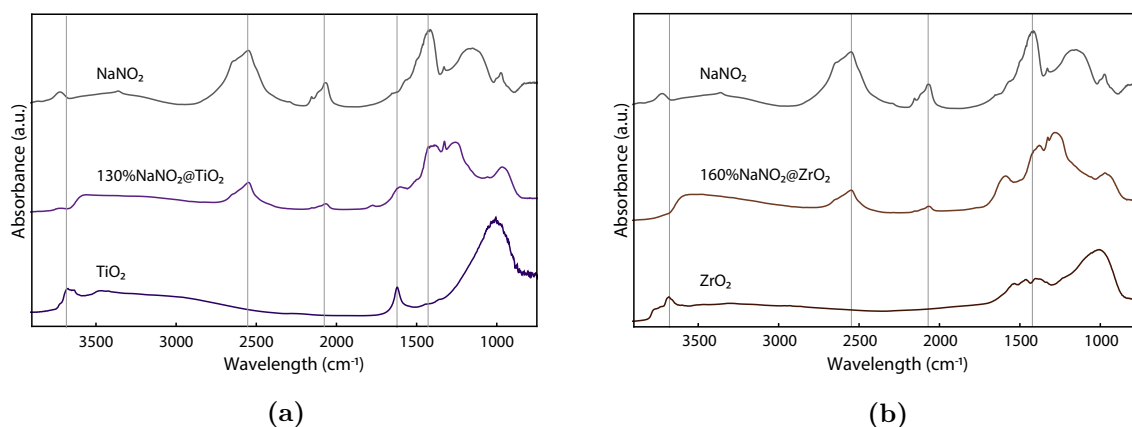


Figure 6.3: (a) DRIFTS of the $\text{NaNO}_2@\text{TiO}_2$ nanocomposite (b) DRIFTS of the $\text{NaNO}_2@\text{ZrO}_2$ nanocomposite

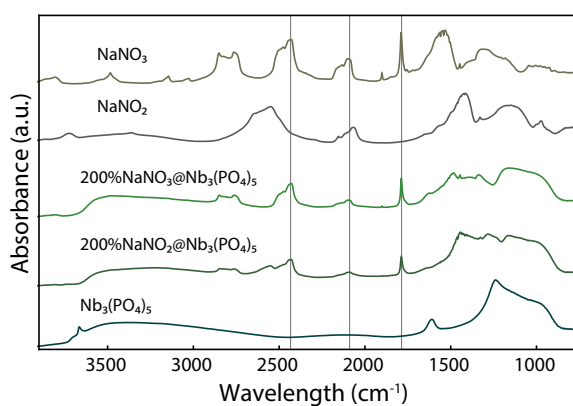


Figure 6.4: DRIFTS of the $\text{NaNO}_2@\text{Nb}_3(\text{PO}_4)_5$ and $\text{NaNO}_3@\text{Nb}_3(\text{PO}_4)_5$ nanocomposites

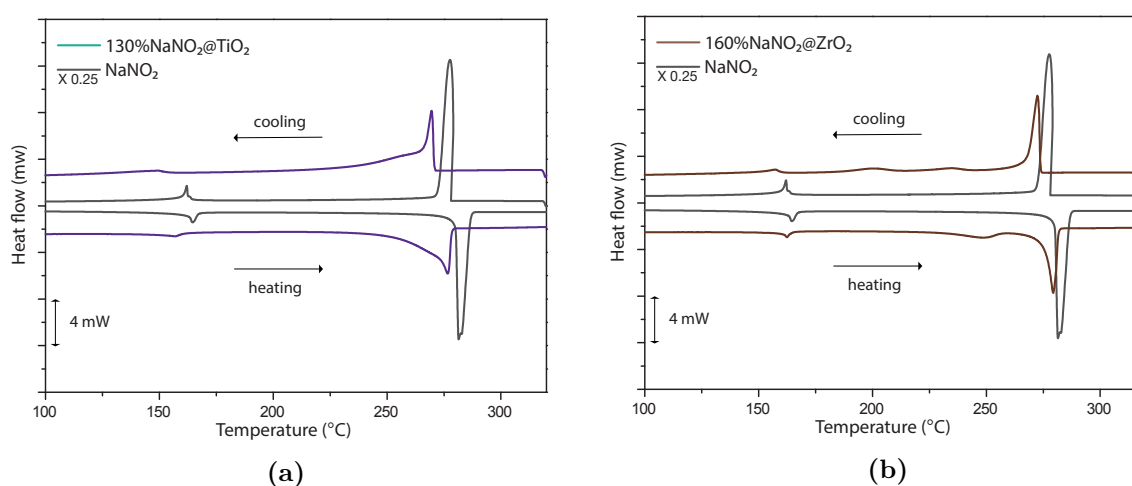


Figure 6.5: (a) DSC of the $\text{NaNO}_2@\text{TiO}_2$ nanocomposite (b) DSC of the $\text{NaNO}_2@\text{ZrO}_2$ nanocomposite

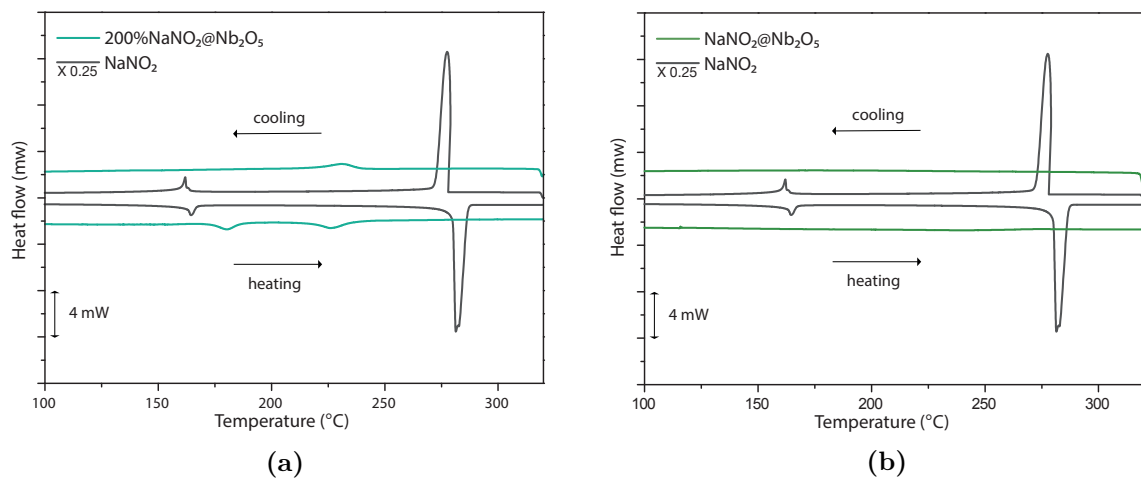


Figure 6.6: (a) DSC of the $\text{NaNO}_2@\text{Nb}_3\text{O}_5$ nanocomposite (b) DSC of the $\text{NaNO}_2@\text{Nb}_3(\text{PO}_4)_5$ nanocomposite

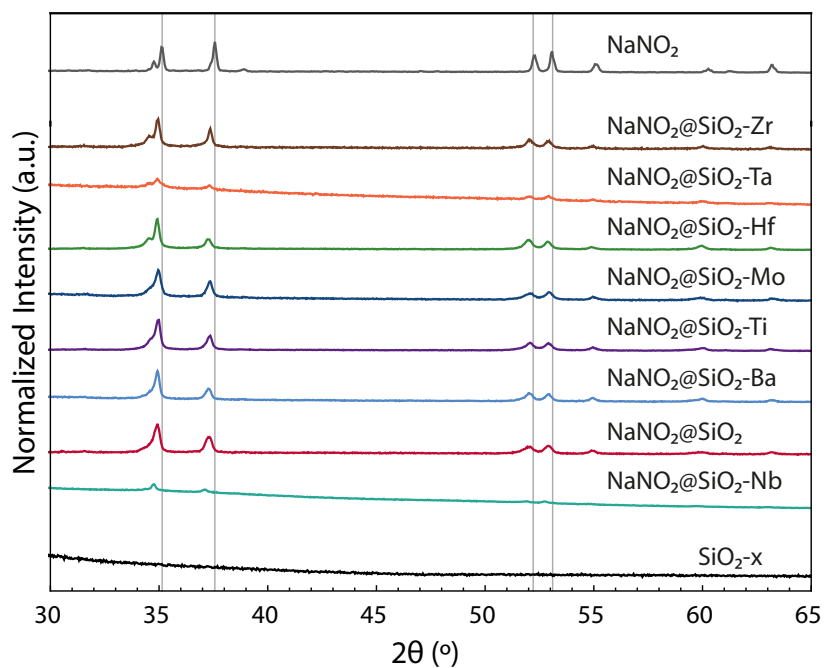


Figure 6.7: XRD of $\text{NaNO}_2@\text{SiO}_2\text{-x}$ nanocomposites

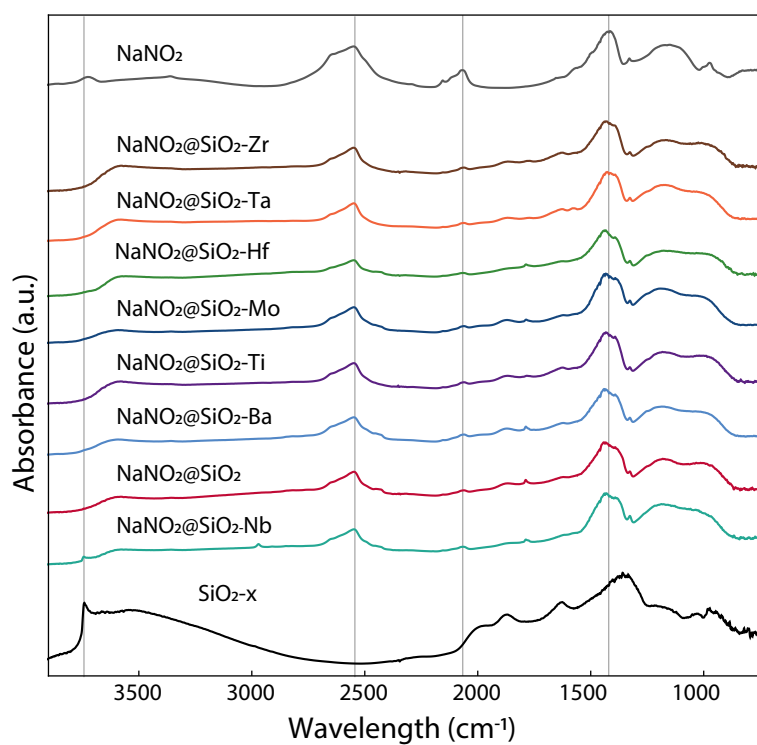


Figure 6.8: DRIFTS of $\text{NaNO}_2@\text{SiO}_2\text{-x}$ nanocomposites

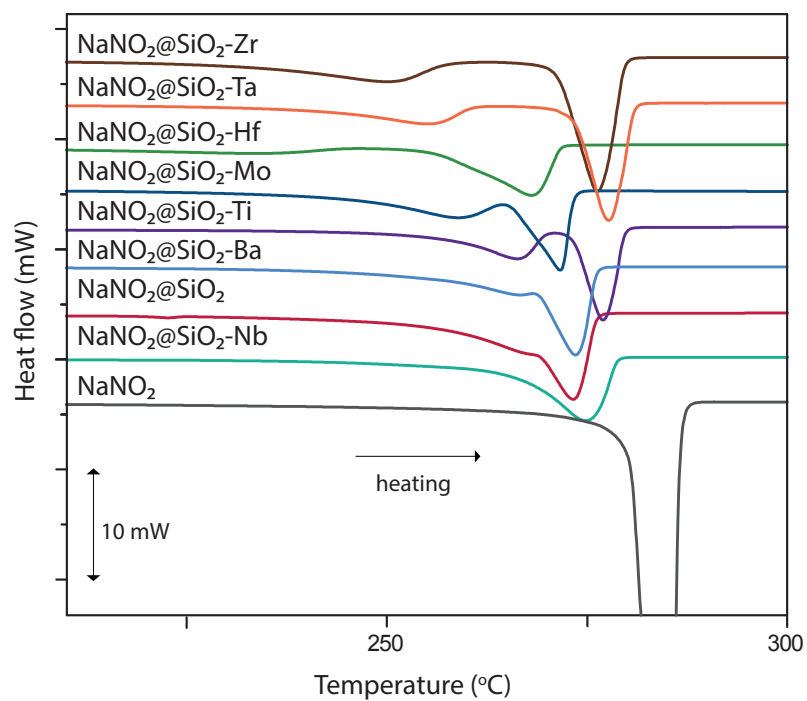


Figure 6.9: DSC of $\text{NaNO}_2@\text{SiO}_2\text{-x}$ nanocomposites

6.1.2 NaNO_3

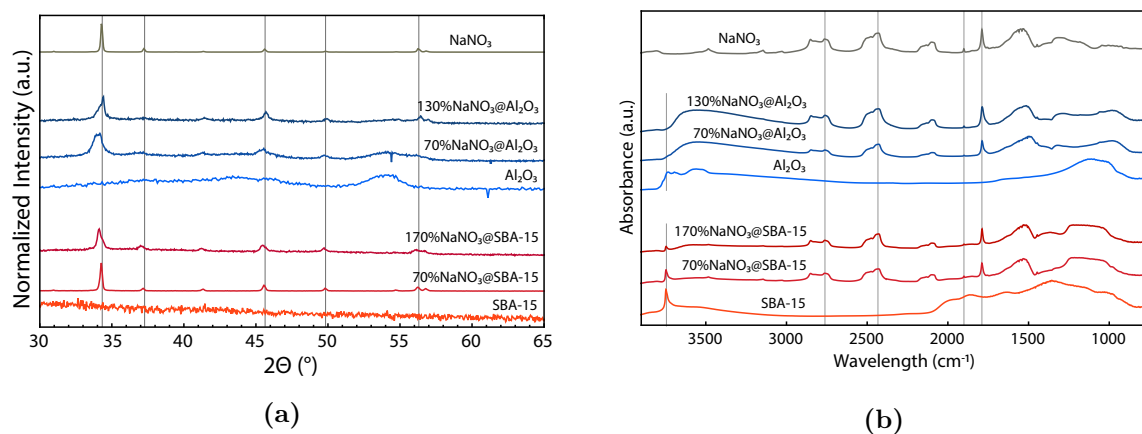


Figure 6.10: (a) XRD of the $\text{NaNO}_3@\text{SBA-15}$ and $\text{NaNO}_3@\text{Al}_2\text{O}_3$ nanocomposites (b) DRIFTS of the $\text{NaNO}_3@\text{SBA-15}$ and $\text{NaNO}_3@\text{Al}_2\text{O}_3$ nanocomposites

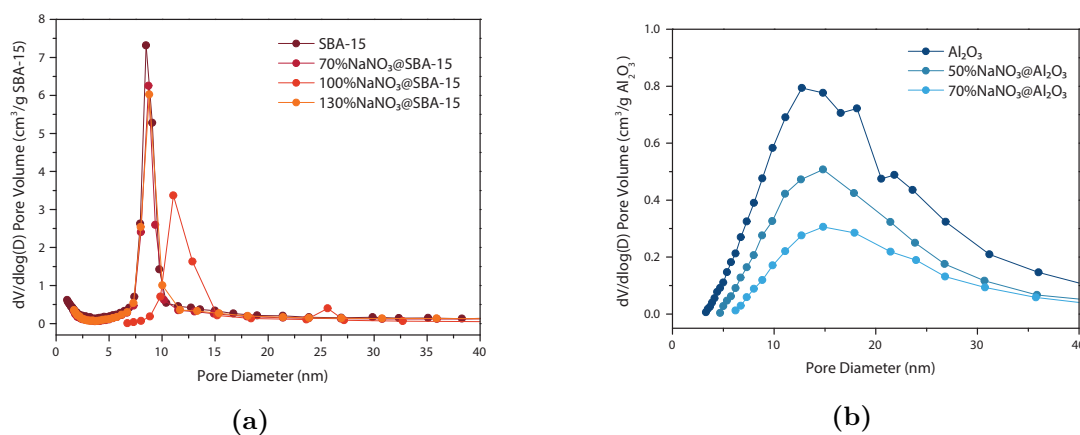


Figure 6.11: (a) Pore size distribution of SBA-15 and $\text{NaNO}_3@\text{SBA-15}$ nanocomposites (b) Pore size distribution of Al_2O_3 and $\text{NaNO}_3@\text{Al}_2\text{O}_3$ nanocomposites

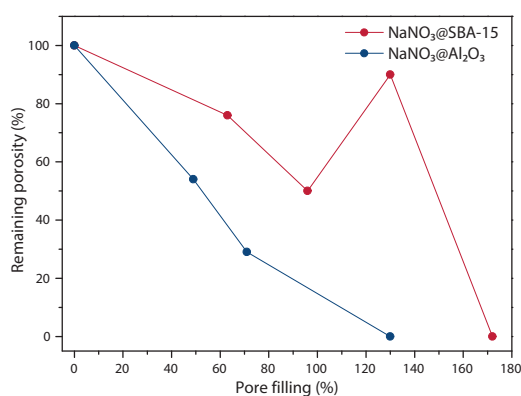


Figure 6.12: Trends in remaining porosity of $\text{NaNO}_3@\text{SBA-15}$ and $\text{NaNO}_3@\text{Al}_2\text{O}_3$ nanocomposites of different pore fillings

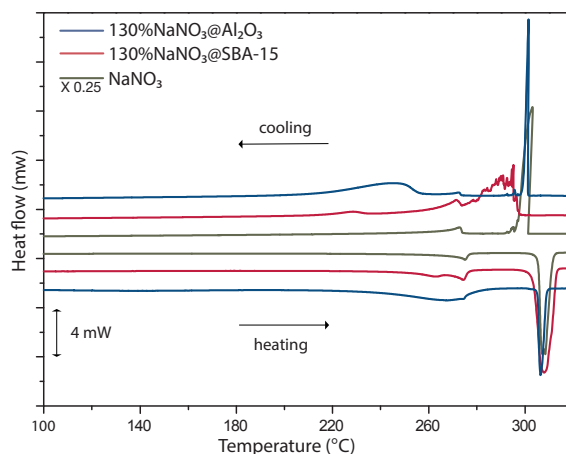


Figure 6.13: DSC of the $\text{NaNO}_3@\text{SBA-15}$ and $\text{NaNO}_3@\text{Al}_2\text{O}_3$ nanocomposites

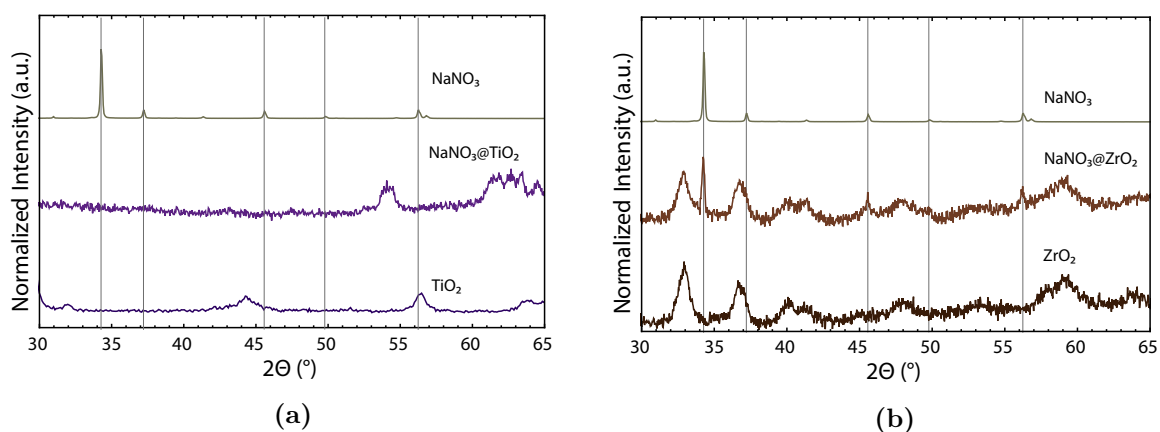


Figure 6.14: (a) XRD of the $\text{NaNO}_3@\text{TiO}_2$ nanocomposite (b) XRD of the $\text{NaNO}_3@\text{ZrO}_2$ nanocomposite

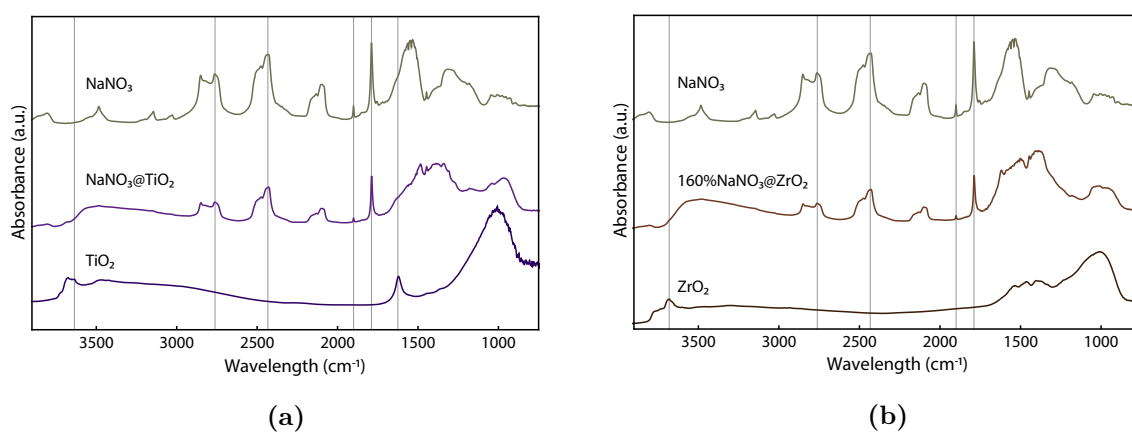
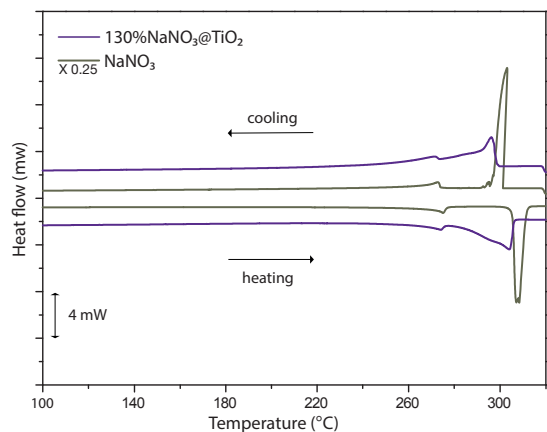
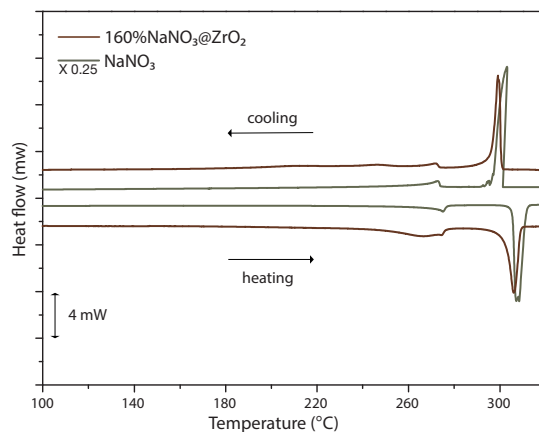


Figure 6.15: (a) DRIFTS of the $\text{NaNO}_3@\text{TiO}_2$ nanocomposite (b) DRIFTS of the $\text{NaNO}_3@\text{ZrO}_2$ nanocomposite

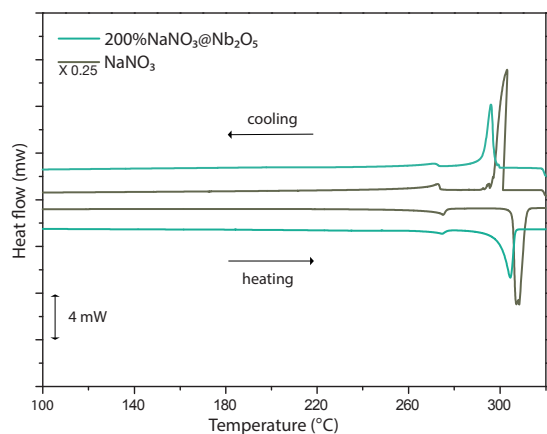


(a)

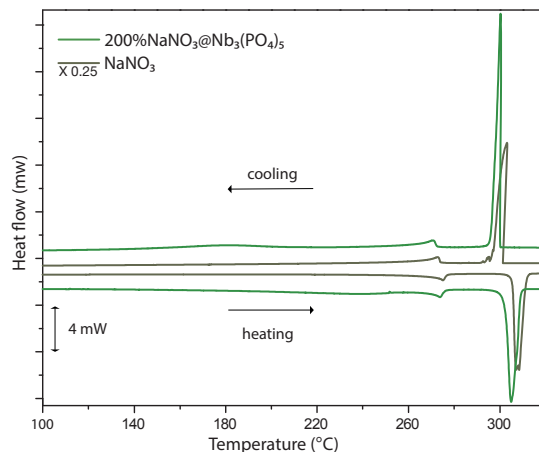


(b)

Figure 6.16: (a) DSC of the $\text{NaNO}_3@\text{TiO}_2$ nanocomposite (b) DSC of the $\text{NaNO}_3@\text{ZrO}_2$ nanocomposite



(a)



(b)

Figure 6.17: (a) DSC of the $\text{NaNO}_3@\text{Nb}_2\text{O}_5$ nanocomposite (b) DSC of the $\text{NaNO}_3@\text{Nb}_3(\text{PO}_4)_5$ nanocomposite

6.2 B: List of samples

Sample name	Date	Chemical composition	Preparation
MvI01	17-12-2018	Mg(BH ₄) ₂ @MCM-41	melt infiltration, H ₂ pressure
MvI02	17-12-2018	Mg(BH ₄) ₂ @OXO-70	melt infiltration, H ₂ pressure
MvI03	7-1-2019	Mg(OH) ₂ @TiO ₂ P90	melt infiltration
MvI04	7-1-2019	Mg(OH) ₂ @TiO ₂ r_450 (PN)	melt infiltration
MvI05	15-1-2019	Mg(BH ₄) ₂ + TiO ₂ P90	physical mixture
MvI06	15-1-2019	Mg(BH ₄) ₂ + Zn(OH) ₂	physical mixture
MvI07	22-1-2019	Mg(ClO ₄) ₂ + TiO ₂ r450 (MvI)	physical mixture
MvI08	23-1-2019	Mg(stearate) + TiO ₂ r450 (MvI)	physical mixture
MvI09	3-5-2019	NaNO ₃ @Aerosil300	melt infiltration
MvI09	3-5-2019	NaNO ₃ @Aerosil300	melt infiltration
MvI10	3-5-2019	NaNO ₃ @AerosilR812	melt infiltration
MvI11	6-5-2019	NaNO ₂ @Aerosil300	melt infiltration
MvI12	6-5-2019	NaNO ₂ @AerosilR812	melt infiltration
MvI13	13-5-2019	NaNO ₃ @AerosilR812	melt infiltration
MvI14	15-5-2019	NaNO ₃ @SBA-15-CH ₃	melt infiltration
MvI15	15-5-2019	NaNO ₃ @SBA-15-NH ₂	melt infiltration
MvI16	15-5-2019	NaNO ₃ @SBA-15	melt infiltration
	22-5-2019	NaNO ₃ control	melting
MvI17	28-5-2019	170% NaNO ₃ @SBA-15-CH ₃	melt infiltration
MvI18	28-5-2019	170% NaNO ₃ @SBA-15-NH ₂	melt infiltration
MvI19	28-5-2019	170% NaNO ₃ @SBA-15	melt infiltration
MvI20	12-6-2019	70% NaNO ₃ @SBA-15	melt infiltration
MvI21	12-6-2019	100% NaNO ₃ @SBA-15	melt infiltration
MvI22	14-6-2019	NaNO ₂ @Al ₂ O ₃ _ox070	melt infiltration, Ar pressure
MvI23	14-6-2019	NaNO ₂ @Al ₂ O ₃ _400	melt infiltration, Ar pressure
MvI24	14-6-2019	NaNO ₂ @Al ₂ O ₃ _500	melt infiltration, Ar pressure
MvI25	14-6-2019	NaNO ₃ @Al ₂ O ₃ _500	melt infiltration, Ar pressure
MvI26	26-6-2019	NaNO ₂ @Al ₂ O ₃ _500	melt infiltration, Ar pressure
MvI27	26-6-2019	NaNO ₂ @Al ₂ O ₃ _600	melt infiltration, Ar pressure
MvI28	26-6-2019	NaNO ₃ @Al ₂ O ₃ _400	melt infiltration, Ar pressure
MvI29	26-6-2019	NaNO ₃ @Al ₂ O ₃ _600	melt infiltration, Ar pressure
MvI30	27-6-2019	NaNO ₂ @Al ₂ O ₃ _200	melt infiltration, Ar pressure
MvI31	27-6-2019	NaNO ₂ @Al ₂ O ₃ _300	melt infiltration, Ar pressure
MvI32	27-6-2019	NaNO ₃ @Al ₂ O ₃ _200	melt infiltration, Ar pressure
MvI33	27-6-2019	NaNO ₃ @Al ₂ O ₃ _300	melt infiltration, Ar pressure
MvI34	17-7-2019	NaNO ₃ @Al ₂ O ₃ _ox070	melt infiltration, Ar pressure
MvI35	17-7-2019	NaNO ₂ @SBA-15 (170%)	melt infiltration, Ar pressure
MvI36	17-7-2019	NaNO ₂ @TiO ₂ p90	melt infiltration, Ar pressure
MvI37	17-7-2019	NaNO ₃ @TiO ₂ p90	melt infiltration, Ar pressure
MvI38	26-7-2019	50% NaNO ₂ @Al ₂ O ₃ _200	melt infiltration, Ar pressure
MvI39	26-7-2019	70% NaNO ₂ @Al ₂ O ₃ _200	melt infiltration, Ar pressure
MvI40	26-7-2019	50% NaNO ₃ @Al ₂ O ₃ _200	melt infiltration, Ar pressure
MvI41	26-7-2019	70% NaNO ₃ @Al ₂ O ₃ _200	melt infiltration, Ar pressure
MvI42	29-7-2019	NaNO ₂ @TiO ₂ _r100	melt infiltration, Ar pressure
MvI43	29-7-2019	NaNO ₃ @TiO ₂ _r100	melt infiltration, Ar pressure

MvI44	27-8-2019	NaNO ₂ @TiO ₂ (MP)	melt infiltration, Ar pressure
MvI45	27-8-2019	NaNO ₂ @TiO ₂ -r450 (MvI)	melt infiltration, Ar pressure
MvI46	27-8-2019	NaNO ₂ @Nb ₂ O ₅ *H ₂ O	melt infiltration, Ar pressure
MvI47	27-8-2019	NaNO ₂ @Nb ₃ (PO ₄) ₅	melt infiltration, Ar pressure
MvI48	2-9-2019	200%NaNO ₂ @Nb ₂ O ₅	melt infiltration, Ar pressure
MvI49	2-9-2019	200%NaNO ₂ @Nb ₃ (PO ₄) ₅	melt infiltration, Ar pressure
MvI50	2-9-2019	80% NaNO ₂ /20% NaNO ₃	melt infiltration, Ar pressure
MvI51	2-9-2019	80% NaNO ₂ /20% NaNO ₃ @Al ₂ O ₃ -ox070	melt infiltration, Ar pressure
MvI52	9-9-2019	2.35NaNO@Nb ₂ O ₅	melt infiltration, Ar pressure
MvI53	9-9-2019	2.35NaNO ₂ @Nb ₃ (PO ₄) ₅	melt infiltration, Ar pressure
MvI54	9-9-2019	2.35NaNO ₂ @ZrO ₂	melt infiltration, Ar pressure
MvI55	9-9-2019	2.35NaNO ₂ @ZnO	melt infiltration, Ar pressure
sMvI56	24-9-2019	250%NaNO ₂ @Nb ₂ O ₃	melt infiltration, Ar pressure
MvI57	24-9-2019	300%NaNO ₂ @Nb ₂ O ₃	melt infiltration, Ar pressure
MvI58	24-9-2019	50%NaNO ₂ @SBA-15	melt infiltration, Ar pressure
MvI59	24-9-2019	70%NaNO ₂ @SBA-15	melt infiltration, Ar pressure
MvI60	26-9-2019	10%NaNO ₂ @SBA-15	melt infiltration, Ar pressure
MvI61	26-9-2019	130%NaNO ₂ @SBA-15	melt infiltration, Ar pressure
MvI62	26-9-2019	10%NaNO ₂ @Al ₂ O ₃ -200	melt infiltration, Ar pressure
MvI63	26-9-2019	130%NaNO ₂ @Al ₂ O ₃ -200(2)	melt infiltration, Ar pressure
MvI64	21-10-2019	100%NaNO ₂ @Al ₂ O ₃ -200	melt infiltration, Ar pressure
MvI65	21-10-2019	110%NaNO ₂ @Al ₂ O ₃ -200	melt infiltration, Ar pressure
MvI66	21-10-2019	120%NaNO ₂ @Al ₂ O ₃ -200	melt infiltration, Ar pressure
MvI67	21-10-2019	150%NaNO ₂ @Al ₂ O ₃ -200	melt infiltration, Ar pressure
MvI68	22-10-2019	200%NaNO ₃ @Nb ₂ O ₅	melt infiltration, Ar pressure
MvI69	22-10-2019	200%NaNO ₂ /NaNO ₃ @Nb ₂ O ₅	melt infiltration, Ar pressure
MvI70	4-11-2019	NaNO ₂ @SiO ₂ 1404	melt infiltration, Ar pressure
MvI71	4-11-2019	NaNO ₂ @SiO ₂ -Hf	melt infiltration, Ar pressure
MvI72	4-11-2019	NaNO ₂ @SiO ₂ -Zr	melt infiltration, Ar pressure
MvI73	4-11-2019	NaNO ₂ @SiO ₂ -Ti	melt infiltration, Ar pressure
MvI74	11-11-2019	NaNO ₂ @SiO ₂ -Mo	melt infiltration, Ar pressure
MvI75	11-11-2019	NaNO ₂ @SiO ₂ -Nb	melt infiltration, Ar pressure
MvI76	11-11-2019	NaNO ₂ @SiO ₂ -Ta	melt infiltration, Ar pressure
MvI77	11-11-2019	NaNO ₂ @SiO ₂ -V	melt infiltration, Ar pressure
MvI78	19-11-2019	NaNO ₂ @SiO ₂ -Ba	melt infiltration, Ar pressure
MvI79	19-11-2019	NaNO ₂ @Al ₂ O ₃ -200	melt infiltration, Ar pressure
MvI80	19-11-2019	2.35NaNO ₃ @Nb ₃ (PO ₄) ₅	melt infiltration, Ar pressure
MvI81	19-11-2019	2.35NaNO ₃ @ZrO ₂	melt infiltration, Ar pressure
		NaNO ₂ control	
		NaNO ₃ control	
MvI B01	5-11-2019	130%NaNO ₂ @Al ₂ O ₃ -200	Ball milling
MvI B02	5-11-2019	200%NaNO ₂ @Nb ₂ O ₅	Ball milling
MvI B03	5-11-2019	130%NaNO ₂ @TiO ₂	Ball milling
MvI B04	5-11-2019	170%NaNO ₂ @SBA-15	Ball milling
MvI B05	5-11-2019	60/40 NaNO ₂ /Al ₂ O ₃ -200	Ball milling
MvI B06	5-11-2019	60/40 NaNO ₂ /Nb ₂ O ₅	Ball milling
MvI B07	5-11-2019	60/40 NaNO ₂ /TiO ₂	Ball milling
MvI B08	5-11-2019	60/40 NaNO ₂ /SBA-15	Ball milling
MvI B09	5-11-2019	NaNO ₂	Ball milling

6.3 D: Excluded experiments

Project	Nanocomposite	Reason for exclusion
Magnesium	$\text{Mg}(\text{BH}_4)_2@\text{MCM-41}$ $\text{Mg}(\text{BH}_4)_2@\text{Al}_2\text{O}_3$ $\text{Mg}(\text{OH})_2@\text{TiO}_2$ $\text{Mg}(\text{OH})_2@\text{TiO}_2$ (red@450 °C) $\text{Mg}(\text{BH}_4)_2+\text{TiO}_2$ $\text{Mg}(\text{BH}_4)_2+\text{Zn}(\text{OH})_2$ $\text{Mg}(\text{ClO})_4+\text{TiO}_2$ (red@450 °C) $\text{Mg}(\text{stereate})+\text{TiO}_2$ (red@450 °C)	It is impossible to make pellets where the nanocomposite is in good contact with the dye, since magnesium foil does not excists. EIS measurement give very low conductivity. It is impossible to determine whether this is due to the bad interface or whether the material is a bad conductor.
Aerosils	$\text{NaNO}_2@\text{Aerosil300}$ $\text{NaNO}_2@\text{AerosilR812}$ $\text{NaNO}_3@\text{Aerosil300}$ $\text{NaNO}_3@\text{AerosilR812}$	It was impossible to make pellet to measure conductivity. The powder did not stick together.
Surface modified SBA-15	$\text{NaNO}_3@\text{SBA-15-CH}_3$ $\text{NaNO}_3@\text{SBA-15-NH}_2$	It was impossible to make pellet to measure conductivity. The powder did not stick together.
Heat treated Alumina	$\text{NaNO}_2@\text{Al}_2\text{O}_3\text{-300}$ $\text{NaNO}_2@\text{Al}_2\text{O}_3\text{-400}$ $\text{NaNO}_2@\text{Al}_2\text{O}_3\text{-500}$ $\text{NaNO}_2@\text{Al}_2\text{O}_3\text{-600}$ $\text{NaNO}_3@\text{Al}_2\text{O}_3\text{-300}$ $\text{NaNO}_3@\text{Al}_2\text{O}_3\text{-400}$ $\text{NaNO}_3@\text{Al}_2\text{O}_3\text{-500}$ $\text{NaNO}_3@\text{Al}_2\text{O}_3\text{-600}$	The heat treatment did not change the alumina significantly. The conductivities of the nanocomposites were within one order of magnitude.
reduced TiO_2	$\text{NaNO}_2@\text{TiO}_2\text{-red}@100\text{ °C}$ $\text{NaNO}_3@\text{TiO}_2\text{-red}@100\text{ °C}$ $\text{NaNO}_2@\text{TiO}_2\text{-red}@450\text{ °C}$	Reducing TiO_2 before using it as a scaffold for nanocomposites did not change/increase the conductivity of the nanocomposites
Ball milling	$\text{NaNO}_2@\text{Al}_2\text{O}_3\text{-200}$ $\text{NaNO}_2@\text{Nb}_2\text{O}_5$ $\text{NaNO}_2@\text{TiO}_2$ $\text{NaNO}_2@\text{SBA-15}$	Ball mill samples were made, but there was no time left to analyse them.